



NAVAL POSTGRADUATE SCHOOL

MONTEREY, CALIFORNIA

THESIS

**IMPACTS OF POTENTIAL AIRCRAFT OBSERVATIONS
ON FORECASTS OF TROPICAL CYCLONES OVER THE
WESTERN NORTH PACIFIC**

by

Mark C. Mitchell

December 2014

Thesis Co-Advisors:

Patrick A. Harr
Wendell Nuss

Approved for public release; distribution is unlimited

THIS PAGE INTENTIONALLY LEFT BLANK

REPORT DOCUMENTATION PAGE			<i>Form Approved OMB No. 0704-0188</i>	
Public reporting burden for this collection of information is estimated to average 1 hour per response, including the time for reviewing instruction, searching existing data sources, gathering and maintaining the data needed, and completing and reviewing the collection of information. Send comments regarding this burden estimate or any other aspect of this collection of information, including suggestions for reducing this burden, to Washington headquarters Services, Directorate for Information Operations and Reports, 1215 Jefferson Davis Highway, Suite 1204, Arlington, VA 22202-4302, and to the Office of Management and Budget, Paperwork Reduction Project (0704-0188) Washington DC 20503.				
1. AGENCY USE ONLY (Leave blank)		2. REPORT DATE December 2014	3. REPORT TYPE AND DATES COVERED Master's Thesis	
4. TITLE AND SUBTITLE IMPACTS OF POTENTIAL AIRCRAFT OBSERVATIONS ON FORECASTS OF TROPICAL CYCLONES OVER THE WESTERN NORTH PACIFIC			5. FUNDING NUMBERS	
6. AUTHOR(S) Mark C. Mitchell				
7. PERFORMING ORGANIZATION NAME(S) AND ADDRESS(ES) Naval Postgraduate School Monterey, CA 93943-5000			8. PERFORMING ORGANIZATION REPORT NUMBER	
9. SPONSORING /MONITORING AGENCY NAME(S) AND ADDRESS(ES) N/A			10. SPONSORING/MONITORING AGENCY REPORT NUMBER	
11. SUPPLEMENTARY NOTES The views expressed in this thesis are those of the author and do not reflect the official policy or position of the Department of Defense or the U.S. Government. IRB protocol number ____N/A____.				
12a. DISTRIBUTION / AVAILABILITY STATEMENT Approved for public release; distribution is unlimited			12b. DISTRIBUTION CODE A	
13. ABSTRACT (maximum 200 words) A goal of The Observing System Research and Predictability Experiment (THORPEX) Pacific Asian Regional Campaign (T-PARC) that was conducted in 2008 over the western North Pacific was to examine the targeted observation for improving initial conditions of numerical forecasts of typhoon track and intensity. Results indicated that observation impacts depended on the location of the observation with respect to the storm and the altitude from which the observation provided a profile of winds, temperature, and moisture. In this thesis, the experiment results were augmented by testing the impact of observations that could potentially be obtained from an unmanned Global Hawk aircraft taking observations over the large-scale environment from an altitude that provided for profiles of the entire troposphere. The case of Typhoon Sinlaku is used as operational typhoon track forecast scenarios were highly uncertain and research-based aircraft observations were available to test against the pseudo Global Hawk observations. Three numerical experiments are conducted such that initial conditions were based on conventional observations, conventional and inner-storm aircraft observations and conventional and pseudo Global Hawk observations. Inclusion of pseudo Global Hawk observations resulted in the most accurate intensity forecasts but track forecasts were best using observations of the storm inner core.				
14. SUBJECT TERMS Global Hawk, Tropical Cyclone Reconnaissance, Observations, Data Assimilation, Numerical Weather Prediction, Typhoon, Recurve, Tropical Northern West Pacific			15. NUMBER OF PAGES 89	
			16. PRICE CODE	
17. SECURITY CLASSIFICATION OF REPORT Unclassified	18. SECURITY CLASSIFICATION OF THIS PAGE Unclassified	19. SECURITY CLASSIFICATION OF ABSTRACT Unclassified	20. LIMITATION OF ABSTRACT UU	

THIS PAGE INTENTIONALLY LEFT BLANK

Approved for public release; distribution is unlimited

**IMPACTS OF POTENTIAL AIRCRAFT OBSERVATIONS ON FORECASTS OF
TROPICAL CYCLONES OVER THE WESTERN NORTH PACIFIC**

Mark C. Mitchell
Lieutenant, United States Navy
B.B.S, University of Texas at San Antonio, 2004

Submitted in partial fulfillment of the
requirements for the degree of

MASTER OF SCIENCE IN METEOROLOGY AND PHYSICAL OCEANOGRAPHY

from the

**NAVAL POSTGRADUATE SCHOOL
December 2014**

Author: Mark C. Mitchell

Approved by: Patrick A. Harr
Thesis Co-Advisor

Wendell A. Nuss
Thesis Co-Advisor

Wendell A. Nuss
Chair, Department of Meteorology

THIS PAGE INTENTIONALLY LEFT BLANK

ABSTRACT

A goal of The Observing System Research and Predictability Experiment (THORPEX) Pacific Asian Regional Campaign (T-PARC) that was conducted in 2008 over the western North Pacific was to examine the targeted observation for improving initial conditions of numerical forecasts of typhoon track and intensity. Results indicated that observation impacts depended on the location of the observation with respect to the storm and the altitude from which the observation provided a profile of winds, temperature, and moisture.

In this thesis, the experiment results were augmented by testing the impact of observations that could potentially be obtained from an unmanned Global Hawk aircraft taking observations over the large-scale environment from an altitude that provided for profiles of the entire troposphere. The case of Typhoon Sinlaku is used as operational typhoon track forecast scenarios were highly uncertain and research-based aircraft observations were available to test against the pseudo Global Hawk observations. Three numerical experiments are conducted such that initial conditions were based on conventional observations, conventional and inner-storm aircraft observations and conventional and pseudo Global Hawk observations. Inclusion of pseudo Global Hawk observations resulted in the most accurate intensity forecasts but track forecasts were best using observations of the storm inner core.

THIS PAGE INTENTIONALLY LEFT BLANK

TABLE OF CONTENTS

I.	INTRODUCTION.....	1
A.	HISTORY	1
B.	MOTIVATION	2
II.	METHODOLOGY	7
III.	BACKGROUND	15
A.	EVOLUTION OF SINLAKE	15
B.	SYNOPTIC ANALYSIS DURING SINLAKE	24
1.	Sea Level Pressure	24
2.	850 hPa.....	26
3.	500 hPa.....	27
4.	200 hPa.....	27
IV.	OBSERVATION SENSITIVITY EXPERIMENTS.....	29
A.	DETERMINISTIC WRF MODEL (WRF-OPS) SIMULATIONS.....	29
B.	SINLAKE WRF-DA EXPERIMENTS.....	43
1.	Initial Position	43
2.	Mean Wind Steering Flow.....	46
3.	Storm Structure and Intensity	58
V.	CONCLUSION	61
A.	SUMMARY OF FINDINGS	61
B.	RECOMMENDATIONS FOR FURTHER STUDY	63
	LIST OF REFERENCES	65
	INITIAL DISTRIBUTION LIST	69

THIS PAGE INTENTIONALLY LEFT BLANK

LIST OF FIGURES

Figure 1.	Enhanced infra-red MTSAT imagery of TY Sinlaku at 0915 UTC 11 September 2008. The WC-130J flight track is defined by the black line. The DOTSTAR flight track is defined by the red line, and the FALCON flight track is defined by the yellow line. (from T-PARC 2008).....	4
Figure 2.	Track forecasts of TY Sinlaku produced by ECMWF global numerical prediction model based on varying initial conditions. The TC positions are plotted at 12 h intervals. Black solid dots are best-track locations. Squares, upward-pointing triangles, downward-pointing triangles, and circles represent forecast of remote observations, vicinity observations, core observations, and all observations, respectively. Cross markers represents forecast of no observations control experiment. (from Harnisch and Weissmann 2010).....	5
Figure 3.	Sinlaku track comparison where the black, red, green, purple, and blue tracks represent JTWC best track, ECMWF YOTC analysis, ECMWF YOTC forecast, WRF (YOTC) analysis, and WRF-(YOTC forecast), respectively. (See text for details).....	7
Figure 4.	Domain configuration used for the WRF deterministic forecasts and the DART-WRF ensemble data assimilation system. The d01 and d02 labels correspond to the first domain (27-km grid spacing) and second domain (9-km grid spacing), respectively.	8
Figure 5.	Data flow and relationship of ECMWF initial and boundary conditions to WRF forecasts.....	9
Figure 6.	Ensemble data assimilation cycle similar to that used for the DART-WRF simulations (see text for details). The model is represented by the green arrows and the state vector of each ensemble is represented by the blue stars; green tick marks correspond to the model state vector mapped to observation space by the forward operator \mathbf{h} ; red tick marks represent observations, and red curves correspond to the observation probability. The blue tick marks represent ensemble updates provided by the ensemble filter; blue arrows at top right are the increments in observation space, and the model increments correspond to the blue arrows near bottom center. Sources of error associated with each step of the data assimilation cycle are listed in the figure (from Anderson et al. 2009).....	10
Figure 7.	Timeline of TY Sinlaku (2008) forecast experiments conducted in this study relative to available in situ dropwindsondes from the USAF WC-130J flight 0133W (red) and pseudo-dropwindsonde observations from the inner-core region (green, “PSEUDO-1”) and surrounding environment (blue, “PSEUDO-2”). Numbers in parentheses correspond to the number of dropwindsondes for each observation set. The red and green lines at the top of the figure correspond to the integration times of the WRF-ANAL and WRF-OPS deterministic forecasts, respectively. The blue line at the top of the figure indicates the DART-WRF ensemble data assimilation	

	phase (1200 UTC 8 September–0600 UTC 9 September), and the purple line corresponds to the DART-WRF ensemble forecasts.	11
Figure 8.	Wind speed (m s^{-1} , shading and vectors) and geopotential height (m, contours) from the ECMWF analysis at (A) 850 hPa and (B) 200 hPa. Panel (A) is valid at 0000 UTC 9 September 2008, and panel (B) is valid at 0600 UTC 9 September 2008. The black line indicates the pseudo flight track used to derive the pseudo-dropwindsonde observations (white and color-filled circles along the flight track) from the ECMWF analysis. The red-filled dropwindsonde locations in panel (A) indicate the inner-core pseudo-dropwindsondes assimilated at 0000 UTC 9 September, while the blue-filled dropwindsonde locations in panel (B) indicate the environmental pseudo-dropwindsondes assimilated at 0600 UTC 9 September. The starting, middle, and ending times (UTC) are indicated for each pseudo-dropwindsonde set.	13
Figure 9.	The track of TY Sinlaku depicted by intensity such that blue is a tropical disturbance, green is a tropical depression, yellow is a tropical storm, red is a typhoon, and magenta is an extratropical cyclone. The numbers in each circle define the day in September 2008. (From Kitamoto National Institute of Informatics (NII))	15
Figure 10.	Enhanced infrared satellite imagery from MTSAT2 at 1430 UTC 7 September 2008. The black arrow points to an area of deep convection associated with the pre-Sinlaku disturbance. (From T-PARC Catalog)	16
Figure 11.	Water vapor imagery MTSAT at 2157 UTC 9 September, 2008 showing area of deep convection. (From T-PARC Catalog)	17
Figure 12.	Enhanced infrared satellite imagery from MTSAT 2 at 1430 UTC 8 September 2008. (From T-PARC Catalog)	18
Figure 13.	Infrared imagery from MTSAT 2 at (a) 0230 UTC 7 September; (b) 0032 UTC 8 September ; (c) 0030 UTC 9 September; and (d) 2030 UTC 9 September. (From T-PARC Catalog)	19
Figure 14.	Infrared imagery from MTSAT2 at 1730 UTC 10 September (from T-PARC Catalog).	20
Figure 15.	Analyzed OHC (kJ cm^{-2}) valid 0000 UTC 10 September 2008. Circle represents the location of the storm (from the East Asian Seas Nowcast Forecast System (EASNFS)).	20
Figure 16.	Eyewall replacement between 10 and 11 Sept 08 (after TPARC_2008 weather summary).....	21
Figure 17.	Analyzed OHC (kJ cm^{-2}) valid 1800 UTC 12 September 2008 (from T-PARC Catalog and Naval Research Lab East Asian Seas Nowcast / Forecast System (NRL EASNFS)).....	22
Figure 18.	Combined 85 GHz microwave and infrared imagery at (a) 2157 UTC 12 September and (b) 0941 UTC 13 September (from Naval Research).	23
Figure 19.	Observations from Yonaginijima Airport 13 Sep 08 (from TPARC_2008 weather summary).....	23
Figure 20.	Analyzed mean sea level pressure (contours in 2 hPa increments) for 1200 UTC 9 September 2008	25

Figure 21.	Analyzed 850 hPa winds (m s^{-1}) and geopotential height (contours, in 30 m intervals) for 1200 UTC 9 September 2008.....	26
Figure 22.	Analyzed mean sea level pressure at 1200 UTC 9 September 2008. Dashed and solid lines represent 500 hPa and 200 hPa geopotential heights (m), respectively. Wind barbs are at 200 hPa with small barbs representing 5 m s^{-1}	27
Figure 23.	Sinlaku track comparison where the black, red, green, purple, and blue tracks represent JTWC best track, ECMWF YOTC analysis, ECMWF YOTC forecast, WRF (YOTC) analysis, and WRF-(YOTC forecast), respectively.	30
Figure 24.	Sinlaku intensity comparison where the black, red, green, purple, and blue lines represent JTWC best track, ECMWF YOTC analysis, ECMWF YOTC forecast, WRF-ANAL and WRF-OPS, respectively.	31
Figure 25.	JTWC TC warning number 4 from 0600 UTC 9 September 2008 (from JTWC).....	31
Figure 26.	JTWC TC warning number 12 from 0600 UTC 11 September 2008 (from JTWC).....	32
Figure 27.	Analyzed winds (vectors) and speed (m s^{-1} , shaded) at 850 hPa and 850 hPa geopotential heights (m, contours at 20 m intervals). The red vector represents general storm motion. The red and yellow contours represent 1530 m and 1510 m geopotential heights,, respectively, at 1200 UTC 8 September.	33
Figure 28.	Analyzed winds (vectors) and speed (m s^{-1} , shaded) at 500 hPa and 500 hPa geopotential heights (m, contours at 20 m intervals) The red and yellow contours represent 5880 m and 5860 m geopotential heights,, respectively, at 1200 UTC 8 September.	33
Figure 29.	Analyzed winds (vectors) and speed (m s^{-1} , shaded) at 200 hPa and 200 hPa geopotential heights (m, contours at 20 m intervals) The red and yellow contours represent 12,460 m and 12,440 m geopotential heights, respectively, at 1200 UTC 8 September.	34
Figure 30.	WRF-OPS 12-h forecast winds (vectors) and speed (m s^{-1} , shaded) at 850 hPa and 850 hPa geopotential heights (m, contours at 20 m intervals). The red vector represents general storm motion. The red and yellow contours represent 1520m and 1500 m geopotential heights, respectively, at 0000 UTC 9 September.	34
Figure 31.	WRF-OPS 12-h forecast winds (vectors), and speed (m s^{-1} , shaded) at 850 hPa and 850 hPa geopotential heights (m, contours at 20 m intervals) The red and yellow contours represent 1520m and 1500 m geopotential heights, respectively, at 0600 UTC 9 September.....	35
Figure 32.	WRF-OPS 12-h forecast winds (vectors) and speed (m s^{-1} , shaded) at 500 hPa and 500 hPa geopotential heights (m, contours at 20 m intervals) The red and yellow contours represent 5880 m and 5860 m geopotential heights, respectively, at 0600 UTC 9 September.....	36
Figure 33.	WFF-OPS 12-h forecast winds (vectors) and speed (m s^{-1} , shaded) at 200 hPa and 200 hPa geopotential heights (m, contours at 20 m intervals) The	

	red and yellow contours represent 12,460 m and 12,440 m geopotential heights, respectively, at 0600 UTC 9 September.....	36
Figure 34.	WRF-OPS 24-h forecast winds (vectors) and speed (m s^{-1} , shaded) at 850 hPa and 850 hPa geopotential heights (m, contours at 20 m intervals). The red vector indicates general storm motion. The red and yellow contours represent 1520 m and 1500 m geopotential heights, respectively, at 1200 UTC 9 September.	37
Figure 35.	WRF-OPS 24-h forecast winds (vectors) and speed (m s^{-1} , shaded) at 500 hPa and 500 hPa geopotential heights (m, contours at 20 m intervals). The red contour represents 5880 geopotential heights at 1200 UTC 9 September	38
Figure 36.	WRF-OPS 24-h forecast winds (vectors) and speed (m s^{-1} , shaded) at 200 hPa and 200 hPa geopotential heights (m, contours at 20 m intervals). The red and yellow contours represent 12,480 m and 12460 m geopotential heights, respectively, at 1200 UTC 9 September.....	38
Figure 37.	WRF-OPS 36-h forecast winds (vectors) and speed (m s^{-1} , shaded) at 850 hPa and 850 hPa geopotential heights (m, contours at 20 m intervals). The red vector indicates general storm motion. The red and yellow contours represent 1520 m and 1500 m geopotential heights, respectively, at 0000 UTC 10 September.	39
Figure 38.	WRF-OPS 36-h forecast winds (vectors) and speed (m s^{-1} , shaded) at 500 hPa and 500 hPa geopotential heights (m, contours at 20 m intervals). The red and yellow contours represent 5885 m and 5865 m geopotential heights, respectively, at 0000 UTC 10 September.....	40
Figure 39.	WRF-OPS 36-h analyzed winds (vectors), speed (m s^{-1} , shaded) at 200 hPa and 200 hPa geopotential heights (m, contours at 20 m intervals). The yellow contour represents 12,460 m geopotential heights at 0000 UTC 10 September.	40
Figure 40.	WRF-OPS 72-h forecast winds (vectors) and speed (m s^{-1} , shaded) at 850 hPa and 850 hPa geopotential heights (m, contours at 20 m intervals). The red vector indicates general storm motion. The red and yellow contours represent 1500 m and 1480 m geopotential heights, respectively, at 1200 UTC 11 September.	41
Figure 41.	WRF-OPS 72-h forecast winds (vectors) and speed (m s^{-1} , shaded) and 500 hPa geopotential heights (m, contours at 20 m intervals). The red and yellow contours represent 5880 m and 5860 m geopotential heights, respectively, at 1200 UTC 11 September.	42
Figure 42.	WRF-OPS 72-h forecast winds (vectors) and speed (m s^{-1} , shaded) at 200 hPa and 200 hPa geopotential heights (m, contours at 20 m intervals). The red and yellow contours represent 12,480 m and 12,460 m geopotential heights, respectively, at 1200 UTC 11 September.....	42
Figure 43.	Ensemble WRF forecasts from the three WRF-DA experiments. Grey lines are ensemble member forecast tracks for TY Sinlaku. Orange line is the ensemble consensus. Black line is JTWC best track. Red line is ECMWF YOTC analysis. Green line is ECMWF YOTC forecast. Purple	

	line is WRF-ANAL. Blue line is WRF-OPS forecast (no additional observation assimilation). Dots represent potential storm position for the given model in 24 h intervals.....	45
Figure 44.	Vorticity difference WRF-C130 minus WRF-CONV for the 18 h forecast verified at 1500 UTC 9 September. Shading represents relative vorticity differences at 850 hPa [10^{-5} s^{-1}]. Contours represent geopotential height differences [m].....	46
Figure 45.	Average motion of Sinlaku for each WRF model run: WRF-CONV (a), WRF-C130 (b), and WRF-PSEUDO (c). The red line and wind barbs denote wind direction and magnitude in increments of 5 knots.	47
Figure 46.	ECMWF EPS at 1200 UTC 8 September. Pink lines represent ensemble member tracks. (From T-PARC catalog).....	48
Figure 47.	Average wind speed and direction at 300 - 800 hPa level with a 300-500 km (left) and 300-1000 km (right) annulus. The abscissa represents date (MM) and time (HH). The ordinate is the magnitude of the steering flow. The green line and wind barbs denote wind direction and magnitude in increments of 5 knots.	49
Figure 48.	The 24-h forecast winds (vectors) and speed (m s^{-1} , shaded) at 850 hPa and 850 hPa geopotential heights (m, contours at 20 m intervals) that verify at 1200 UTC 9 September from the (a) WRF-C130 and (b)WRF-PSEUDO, and (c) WRF-C130 minus WRF-PSEUDO forecast differences. ...	52
Figure 49.	The 30-h forecast winds (vectors), and speed (m s^{-1} , shaded) at 850 hPa and 850 hPa geopotential heights (m, contours at 20 m intervals) that verifies at 1800 UTC 9 September from the (a) WRF-C130, (b) WRF-PSEUDO, and the (c) WRF-C130 minus WRF-PSEUDO forecast differences	53
Figure 50.	The 36-h forecast winds (vectors) and speed (m s^{-1} , shaded) at 850 hPa and 850 hPa geopotential heights (m, contours at 20 m intervals) that verifies at 0000 UTC 10 September from the (a) WRF-C130, (b) WRF-PSEUDO, and (c) WRF-C130 minus WRF-PSEUDO forecast differences. ...	54
Figure 51.	The 36-h forecast winds (vectors) and speed (m s^{-1} , shaded) at 500 hPa and 500 hPa geopotential heights (m, contours at 20 m intervals) that verify at 0000 UTC 10 September from the (a) WRF-C130, (b) WRF-PSEUDO, and (c) WRF-C130 minus WRF-PSEUDO forecast differences. ...	55
Figure 52.	The 24-h forecast winds (vectors) and speed (m s^{-1} , shaded) at 200 hPa and 200 hPa geopotential heights (m, contours at 20 m intervals) that verify at 1200 UTC 9 September from the (a) WRF-C130, (b) WRF-PSEUDO, and (c) WRF-C130 minus WRF-PSEUDO forecast differences. ...	56
Figure 53.	The 30-h forecast winds (vectors) and speed (m s^{-1} , shaded) at 200 hPa and 200 hPa geopotential heights (m, contours at 20 m intervals) that verify at 1800 UTC 9 September from the (a) WRF-C130, (b) WRF-PSEUDO, and (c) WRF-C130 minus WRF-PSEUDO forecast differences. ...	57
Figure 54.	The 36-h forecast winds (vectors) and speed (m s^{-1} , shaded) at 200 hPa and 200 hPa geopotential heights (m, contours at 20 m intervals) that	

verify at 0000 UTC 10 September from the (a) WRF-C130, (b) WRF-PSEUDO, and (c) WRF-C130 minus WRF-PSEUDO forecast differences. ..58

Figure 55. Forecasts of the intensity of TY Sinlaku intensity for the (a) WRF-CONV, (b) WRF-C130, and (c) WRF-PSEUDO forecasts. The grey lines define the ensemble forecasts and the orange line is the ensemble consensus. The black, red, green, purple, and blue lines represent JTWC best track, ECMWF YOTC analysis, ECMWF YOTC forecast, WRF-ANAL, and WRF-OPS, respectively. The abscissa is date (MM) and time (HH UTC). The ordinate is minimum sea level pressure (hPa) in 5 hPa increments.59

LIST OF ACRONYMS AND ABBREVIATIONS

ASCAT	Advanced scatterometer
CDO	Central dense overcast
DART	Data Assimilation Research Testbed
DLR	Deutsches Zentrum für Luft
DOTSTAR	Drosonde Observations for Typhoon Surveillance near the Taiwan Region
EAKF	Ensemble adjustment Kalman filter
ECMWF	European Center for Medium-Range Weather Forecasts
GH	Global Hawk
IR	Infrared
JTWC	Joint Typhoon Warning Center
LLCC	Low level circulation center
MM5	Fifth generation Penn State Mesoscale Model
NCEP	National Center for Environmental Prediction
NOAA	National Oceanic and Atmospheric Administration
SFMR	Stepped frequency microwave radiometer
TC	Tropical Cyclone
TCFA	Tropical cyclone formation alert
THORPEX	The Observing System Research and Predictability Experiment
T-PARC	THORPEX-Pacific Asian Regional Campaign
TY	Typhoon
UAV	Unmanned Aerial Vehicle
WRF	Advanced Weather Research and Forecasting
WSM6	WRF single moment 6 class
YOTC	Year of Tropical Convection
YSU	Yonsei University

THIS PAGE INTENTIONALLY LEFT BLANK

ACKNOWLEDGMENTS

Special thanks go to Dr. Patrick Harr, Dr. Andy Penny, and Mr. Bob Creasy for their mentorship and guidance as I worked through this thesis. Without the modeling expertise of Andy Penny, patience and thoughtful professionalism of Bob Creasy, and of course, the guiding hand of Dr. Patrick Harr, this thesis would not have been completed.

To my classmates, LCDR Kate the “Professor” Hermsdorfer, LCDR Jen “Class lead” Cline, LCDR Ramone “Swagger” Martinez, LCDR Mike “Caddyshack” Harris, LT Carter “Norm” Johnston, LT Will “the Brain” Sauer, and LT Tom “Adjutant General” Newman, I am grateful for your comradery and mentorship. I could not have had a better group of people to share this experience with.

Most importantly of all, my beloved wife, Victoria Mitchell, and children, Mason, Grant, and Reagan, were always there to put a smile on my face to help me decompress from the day. They provided refuge for which to escape from time-to-time, which was invaluable to my success at Naval Postgraduate School. This achievement is as much theirs as it is mine.

Thanks to all.

THIS PAGE INTENTIONALLY LEFT BLANK

I. INTRODUCTION

A. HISTORY

The mission of U. S. Naval Meteorology and Oceanography Command (METOC) has long been centered on providing warfighters with the very best environmental information they need to make the most informed decision. The goal is to never be surprised by environmental conditions. One of the most severe threats to naval shore-based and afloat resources is tropical cyclones (TCs), which occur over many of the ocean basins in which the U.S. Navy operates. As such, TC reconnaissance, analysis, and forecasting have been stated by USPACOM as essential security components to ensure safety of United States assets and National Security (Stephen, 2010).

The Joint Typhoon Weather Center (JTWC) in Pearl Harbor, Hawaii is responsible for the detection and prediction of the path and strength of TCs over the western north Pacific Ocean, the western south Pacific Ocean, and the north and south Indian Oceans. The JTWC mission is built upon the need to protect U.S. assets, maximize cost efficiencies by balancing risk with mission goals; and supply input to sortie decision-making processes. To achieve these goals, the most accurate estimates of current and future storm positions are required. In addition to forecast accuracy, the uncertainty in forecast positions provides key information under which a decision maker must utilize the forecast. As forecast uncertainty decreases, the amount of geographic area that may be placed into unnecessary warning or TC conditions of readiness (TCCOR) will be decreased.

Much earlier than the advent of electronic computing, Lewis Richardson wrote in 1922 (Richardson 1965) about the challenges associated with numerically integrating the fundamental equations required to produce a very rudimentary time evolution of 500 hPa heights. He wrote, “The two great outstanding difficulties are those connected with the completeness necessary in the initial observations and with the elaborateness of the subsequent process of computing” (Richardson, 1965). The basis of the initial conditions needed to initialize a time integration as defined by Richardson are environmental

observations that did not become routinely available until much later than the seminal work of Richardson (1965), Lorenz (1963) defined the sensitivity of numerical simulations to small variations in the initial conditions upon which the numerical integrations were begun. Lorenz's discovery of large variability that could occur in the final state of a numerical integration when initial condition variability was extremely small lead to the more formal concept to chaos theory (Gleick, 1987). Lorenz's work also lead to the development of ensemble forecasting such that the sensitivity to initial conditions could be exploited to provide an estimate of the uncertainty or predictability associated with a given numerical forecast. Eventually, the concept contributed to ensemble data assimilation (Majumdar and et al., 2001), which can be used to define small, random perturbations in initial conditions based on estimates of observation accuracy and spatial distribution. In this thesis, the impact of data distribution on initial conditions and subsequent forecasts is defined in relation to the problem of forecasting the track of a typhoon over the western North Pacific.

B. MOTIVATION

The goal of this thesis is to build on the program titled The Observing System Research and Predictability EXperiment (THORPEX) and more specifically the THORPEX-Pacific Asian Regional Campaign (T-PARC) that was conducted in the fall of 2008 (Elsberry and Harr 2008). During T-PARC, more than 1500 atmospheric soundings were captured via release of dropwindsondes from multiple aircraft platforms (Weissmann et al., 2011). While the aircraft observations were obtained to provide observations of processes (Raymond and Lopez-Carillo 2011, Montgomery et al. 2010; Sanabia 2010) important to TC formation, structure, and structure change, a significant objective of T-PARC was to examine the value of aircraft observations with regard to the accuracy of TC track forecasts produced by operational numerical forecast models (Harnisch and Weissmann 2010; Weissmann et al. 2011; Chuo et al. 2012, Weissmann et al. 2012). The relative value of observations of TC location, intensity, structure, and large-scale environmental conditions were obtained over regions where these observations are not operationally available.

During T-PARC on 11 September 2008, a three-plane mission (Figure 1) was flown into Typhoon (TY) Sinlaku. At this time, there was considerable uncertainty in the forecast track. For this aircraft observing period, a U.S. Air Force WC-130J aircraft conducted a standard TC reconnaissance mission into the storm center. Flight level for the TC reconnaissance was at 700 hPa from which dropsondes were used to obtain profiles of winds, temperature, and water vapor. The stepped frequency microwave radiometer (SFMR) remotely measured surface wind speeds. From Taiwan, the Dropsonde Observations for Typhoon Surveillance near the Taiwan Region (DOTSTAR) aircraft flew near 200 hPa and deployed dropwindsondes in the immediate vicinity of TY Sinlaku. However, the DOTSTAR aircraft did not fly over the center of the storm. Finally, the Deutsches Zentrum für Luft (DLR) FALCON aircraft flew at 200 hPa over a region poleward of Sinlaku. The purpose of the FALCON flight was to gather observations of the region ahead of the storm and measure the relative strength and positions of the subtropical ridge, the low-level monsoon trough, and an upper-level midlatitude trough.

Harnisch and Weissmann (2010), examined the sensitivity of track forecasts of Sinlaku (Figure 2) produced by the European Center for Medium-Range Weather Forecasts (ECMWF) numerical forecast model to variations in initial conditions based on use of the three aircraft observation sets collectively and individually. In this study, they found that the most accurate forecasts were produced from initial conditions in which DOTSTAR observations from high altitude in the near storm environment were used. These forecasts were more accurate than those in which initial conditions were produced by assimilating the low-level data from the WC-130J flight in the typhoon core or at high altitude in a remote region ahead of the storm as observed using the DLR Falcon. The above example, and several others from T-PARC and other programs provide evidence of the value of *in situ* observations of a TC and the near environment of the TC in producing initial conditions that lead to improve forecasts of the storm position. Furthermore, the results from T-PARC point to the variability in observation value based on location of the observation relative to the TC and to the information with respect to a full profile of the troposphere. However, the only ocean basin in which routine aircraft observations are

taken is the North Atlantic. Over the north Atlantic, the U.S. Air Force 53rd Weather Reconnaissance Squadron obtains observations in the TC core and the National Oceanic and Atmospheric Administration (NOAA) Gulfstream IV obtains observations from high altitudes in the synoptic environment of the storm. Given the sensitivities to observation location and altitude, the objective of this thesis is to examine *potential* improvements to numerical forecasts of TC tracks if observations were available from high altitude in the synoptic environment of a western north Pacific typhoon, where routine observations are not available.

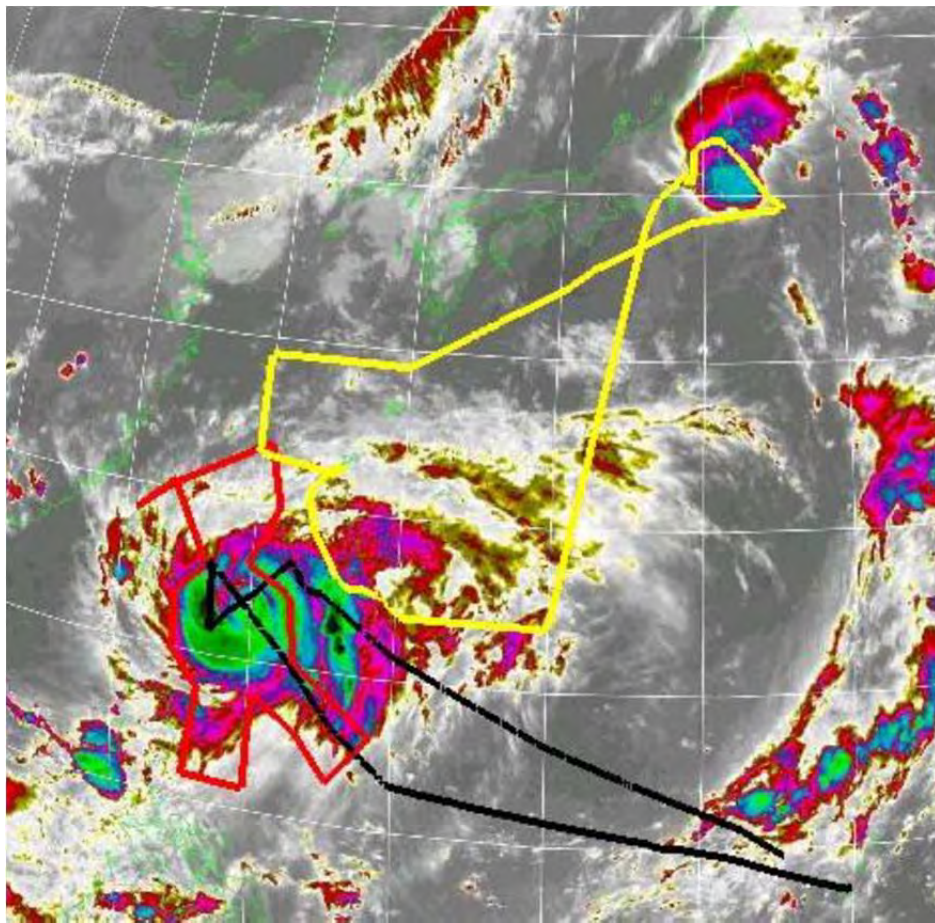


Figure 1. Enhanced infra-red MTSAT imagery of TY Sinlaku at 0915 UTC 11 September 2008. The WC-130J flight track is defined by the black line. The DOTSTAR flight track is defined by the red line, and the FALCON flight track is defined by the yellow line. (from T-PARC 2008)

In this thesis, an experiment is conducted such that simulated dropwindsondes are defined and “deployed” at 60,000 ft as would be conducted from an unmanned aerial vehicle (UAV) such as the Global Hawk (GH). The case of TY Sinlaku during T-PARC is chosen for the experiment because there is a unique set of actual aircraft observations that can be used to define an alternative initial condition to produce a type of benchmark forecast track.

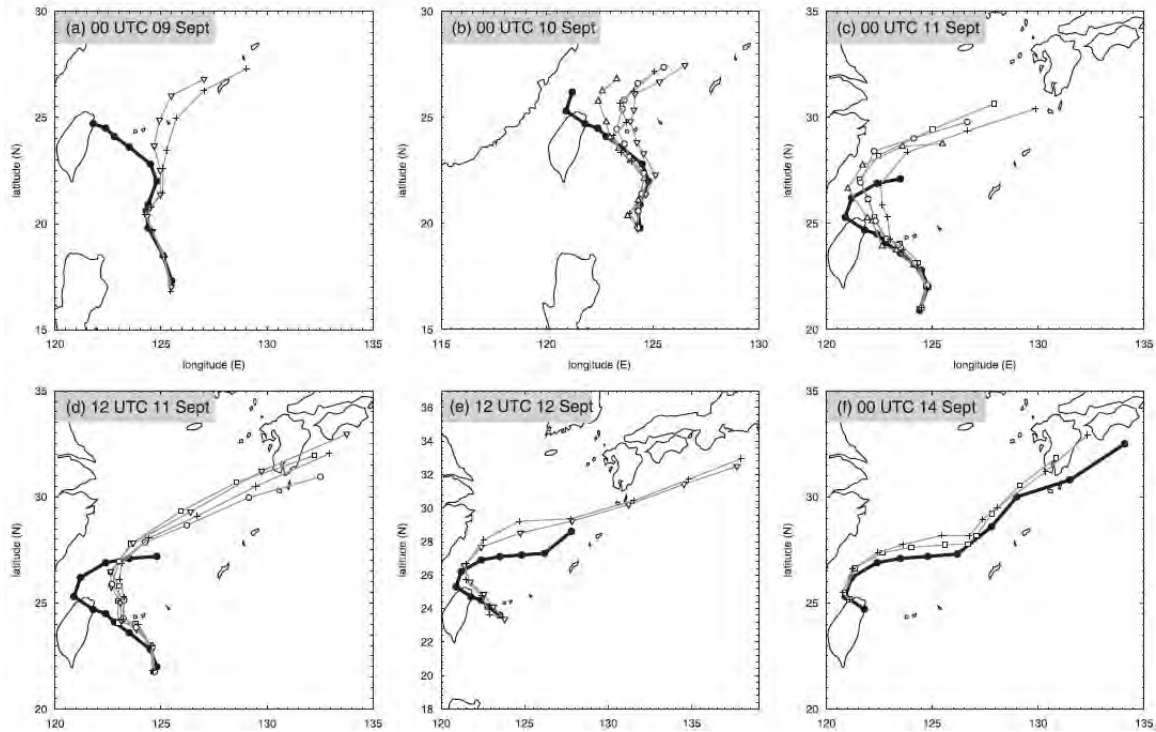


Figure 2. Track forecasts of TY Sinlaku produced by ECMWF global numerical prediction model based on varying initial conditions. The TC positions are plotted at 12 h intervals. Black solid dots are best-track locations. Squares, upward-pointing triangles, downward-pointing triangles, and circles represent forecast of remote observations, vicinity observations, core observations, and all observations, respectively. Cross markers represents forecast of no observations control experiment. (from Harnisch and Weissmann 2010)

The study is outlined as follows. Chapter II details the methodology of the experiment by discussing model parameters, experiment design and execution. Chapter

III provides a background by describing the evolution of Typhoon Sinlaku in September 2008. Chapter IV details the analysis of the experimental model forecasts by comparing and contrasting the various forecasts against a control model run without observation assimilation. Chapter V provides results and follow-on study opportunities.

II. METHODOLOGY

The deterministic and ensemble forecasts of TY Sinlaku were performed using the Advanced Weather Research and Forecasting (WRF-ARW) non-hydrostatic mesoscale model (hereafter WRF) (Skamarock et al. 2008). While Sinlaku existed over the western North Pacific for nearly 2 weeks (Figure 3), this study focuses on the initial 5 days following formation of the storm. During this period, track forecasts were highly variable and Sinlaku underwent significant intensification and structure changes.

Two nested domains (Figure 4) with horizontal grid-spacing of 27- and 9-km and 42 vertical levels were constructed to encompass TY Sinlaku. The near environment microphysical processes were handled using the WRF single moment 6 class (WSM6) microphysics parameterization scheme (Hong and Lim 2006) and cumulus convection was accounted for using the Kain-Fritsch scheme (Fritsch and Kain 1993; Kain 2004). The Yonsei University (YSU) boundary layer scheme (Hong et al. 2006) and fifth generation Penn State Mesoscale Model (MM5) surface layer scheme (Skamarock et al. 2008) were used to represent boundary layer and surface layer processes, respectively.

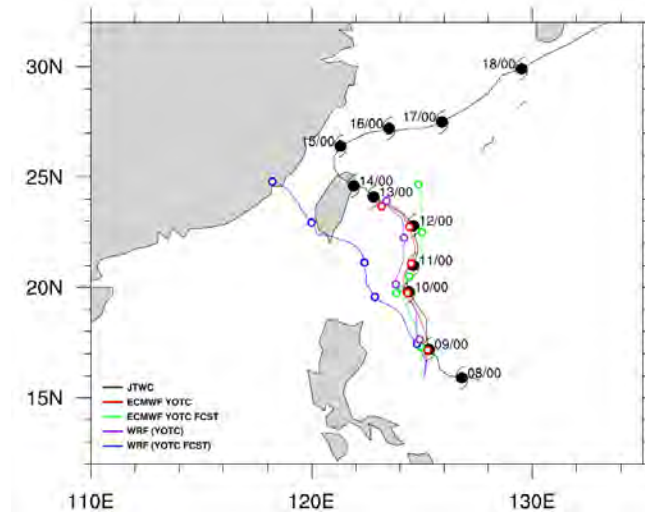


Figure 3. Sinlaku track comparison where the black, red, green, purple, and blue tracks represent JTWC best track, ECMWF YOTC analysis, ECMWF YOTC forecast, WRF (YOTC) analysis, and WRF-(YOTC forecast), respectively. (See text for details)

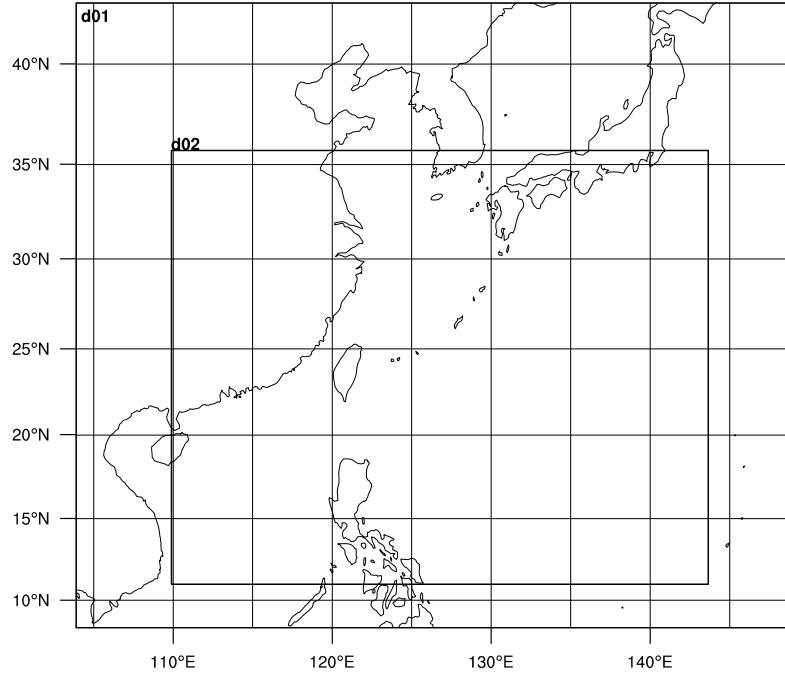


Figure 4. Domain configuration used for the WRF deterministic forecasts and the DART-WRF ensemble data assimilation system. The d01 and d02 labels correspond to the first domain (27-km grid spacing) and second domain (9-km grid spacing), respectively.

Initially, simulations were initialized from the Global Forecast System (GFS) reforecast data (Hamill et al. 2005), however the initial intensity of TY Sinlaku was unrealistically weak in the GFS reforecast data (not shown) such that the deterministic WRF simulation was too slow to develop TY Sinlaku (not shown). In addition, the GFS reforecast data were limited to 36 vertical levels, which was considered too coarse to construct pseudo-dropwindsonde profiles used in the data assimilation aspect of this study. Therefore, the initial and lateral boundary conditions for the WRF deterministic forecast were derived from the ECMWF operational forecast cataloged in the Year of Tropical Convection (YOTC, Waliser et al. 2012) data archive. Therefore, these forecasts initialized at 1200 UTC 8 September are labeled WRF-OPS. It is important to note that the initial conditions for the WRF forecasts derived from the ECMWF operational forecast represented a “best” estimate of the atmospheric state *only* at the initialization time of the global forecast (1200 UTC 8 September), and originated from a blend of the previous forecast and the assimilation of observations available at that time.

A second WRF forecast was generated at the same initial time (1200 UTC 8 September) but boundary conditions were defined from the ECMWF analysis at each update time. Therefore, this forecast is labeled WRF-ANAL and has information not available in real time. The WRF-ANAL forecast serves as a type of upper-bound in accuracy if perfect boundary information would be available. Figure 5 depicts the data flow described above.

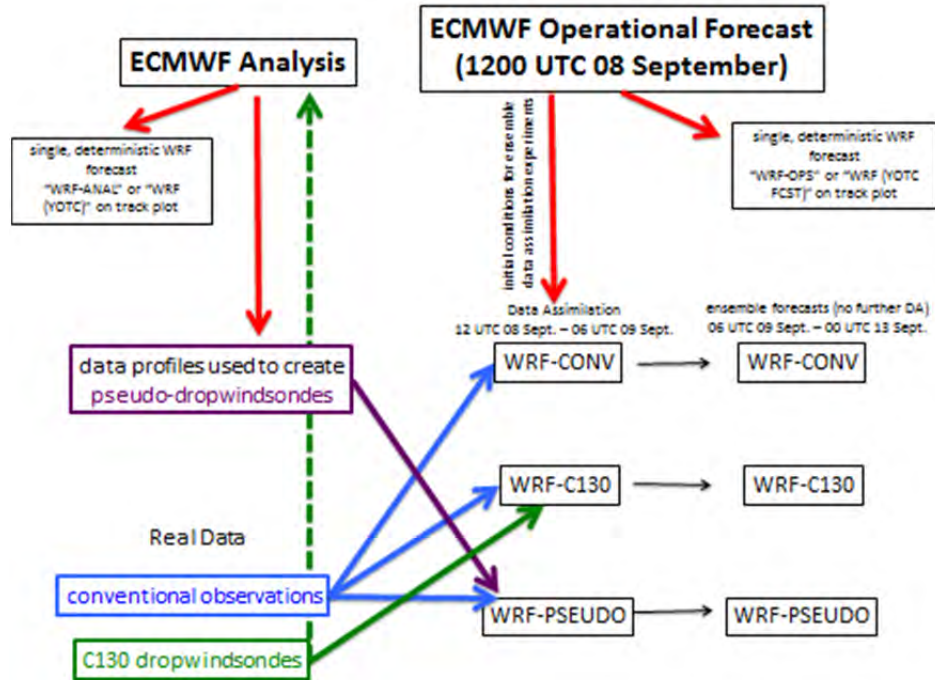


Figure 5. Data flow and relationship of ECMWF initial and boundary conditions to WRF forecasts.

To determine the forecast sensitivity to real and simulated observations, data assimilation (DA) was conducted using the Data Assimilation Research Testbed (DART) (Anderson et al. 2009) ensemble data assimilation system in conjunction with the WRF model (hereafter referred to as DART-WRF). The DART-WRF ensemble was comprised of 48 members that used an identical configuration to the WRF deterministic forecasts described previously.

The DA cycle (Figure 6), which is more generally described in Anderson et al. (2009), is as follows: Observations were assimilated for the period 1200 UTC 8 September - 0600 UTC 9 September 2008 using a 3-h assimilation window (± 90 minutes

centered on the hour). At assimilation time, observations within the ± 90 minute window and their corresponding error characteristics were combined with the ensemble prior state using the ensemble adjustment Kalman filter (EAKF) (Anderson 2003) to generate an increment for each ensemble state. Given the finite ensemble size, which leads to sampling error, spatially varying state-space inflation (Anderson 2007) was also used to increase spread among the ensemble members. The increment was then applied to the ensemble prior state to generate the ensemble posterior state, which was then integrated forward in time by the WRF model until the next assimilation time.

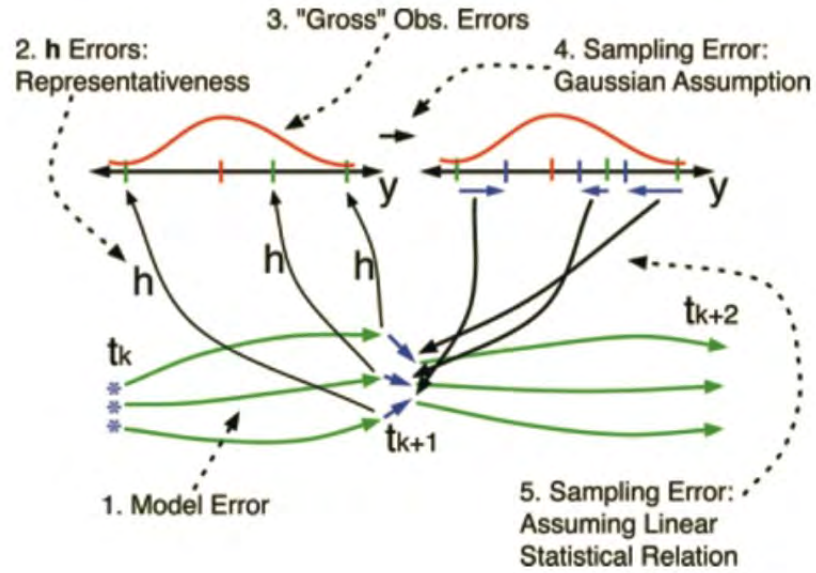


Figure 6. Ensemble data assimilation cycle similar to that used for the DART-WRF simulations (see text for details). The model is represented by the green arrows and the state vector of each ensemble is represented by the blue stars; green tick marks correspond to the model state vector mapped to observation space by the forward operator h ; red tick marks represent observations, and red curves correspond to the observation probability. The blue tick marks represent ensemble updates provided by the ensemble filter; blue arrows at top right are the increments in observation space, and the model increments correspond to the blue arrows near bottom center. Sources of error associated with each step of the data assimilation cycle are listed in the figure (from Anderson et al. 2009).

Three different DA experiments were conducted (Figure 7). The first experiment, hereafter WRF-CONV, only assimilated conventional observations that were available from routine data sources (no *in situ* observations). The second DA experiment, hereafter WRF-C130, assimilated conventional observations as well as dropwindsondes deployed from the USAF WC-130J near 0300 UTC 9 September. The third experiment, hereafter WRF-PSEUDO, assimilated conventional observations and pseudo dropwindsondes generated from gridded ECMWF analysis data (Figure 7). These pseudo-dropwindsonde profiles were created from the ECMWF analysis data by assuming a constant fall velocity of 12 m s^{-1} from a height of 18 km (to roughly match the 60,000 ft cruising altitude of the Global Hawk) while allowing for horizontal advection. Trilinear interpolation was used to define the atmospheric variables at the pseudo-dropwindsonde locations based on the values at surrounding ECMWF grid points. Random normal noise was added to each profile to account for some of the uncertainty since the pseudo-dropwindsonde profiles generated from the gridded model analyses were much ‘smoother’ than actual dropwindsonde profiles (not shown).

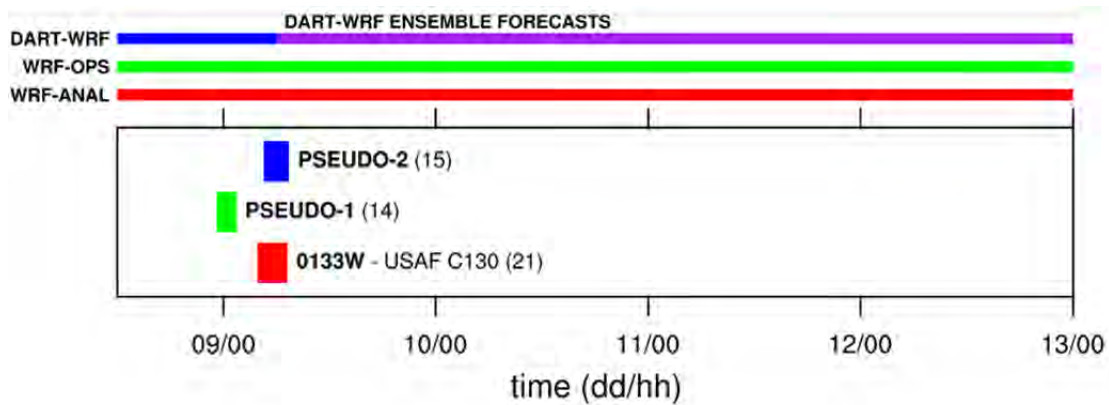


Figure 7. Timeline of TY Sinlaku (2008) forecast experiments conducted in this study relative to available *in situ* dropwindsondes from the USAF WC-130J flight 0133W (red) and pseudo-dropwindsonde observations from the inner-core region (green, “PSEUDO-1”) and surrounding environment (blue, “PSEUDO-2”). Numbers in parentheses correspond to the number of dropwindsondes for each observation set. The red and green lines at the top of the figure correspond to the integration times of the WRF-ANAL and WRF-OPS deterministic forecasts, respectively. The blue line at the top of the figure indicates the DART-WRF ensemble data assimilation phase (1200 UTC 8 September–0600 UTC 9 September), and the purple line corresponds to the DART-WRF ensemble forecasts.

Since ECMWF analyses were only available every 6 h, a pseudo flight-plan (Figure 8) was devised based on an assumed cruising speed of 300 kt to fly over the inner core (centered at 0000 UTC 9 September) and through the outflow of the storm and the midlatitude jet to the north (centered at 0600 UTC 9 September). Although pseudo-dropwindsondes were generated for the entire flight plan, only pseudo-dropwindsondes within ± 90 minutes of 0000 UTC (red dots in Figure 8a) and 0600 UTC (blue dots in Figure 8b) 9 September were assimilated. Unfortunately, when pseudo-dropwindsonde data from the inner-core region were assimilated during the 0000 UTC 9 September assimilation time, over half of the ensemble members became numerically unstable near the observation radius of influence boundary. This may have been a result of the data assimilation conforming too heavily to the pseudo dropwindsonde observations near the storm center such that there was a large disparity between the region impacted by the pseudo-dropwindsondes and the area outside the influence of these observations. As a result, only pseudo-dropwindsonde observations from 0600 UTC 9 September (Figure 8b) were assimilated for the WRF-PSEUDO experiment.

Observation error variances for all observations in this study were generated from the National Center for Environmental Prediction (NCEP) lookup-tables based on the pressure or height level of the observation. A Gaspari-Cohn covariance cutoff radius (Gaspari and Cohn 1999) of ~ 630 km was used for all observations, which limited the observational area of impact. To reduce the computational expense, dropwindsonde data (pseudo and *in situ*) were thinned by only retaining every fifth set of observations in the vertical.

After 18 h of data assimilation, each ensemble member for the three sets of experiments was integrated forward in time from its state at 0600 UTC 9 September to 0000 UTC 13 September (for an additional 90 h). To analyze the impact of the different observation sets, the track, intensity, and structure of TY Sinlaku of the three ensemble means were examined and compared.

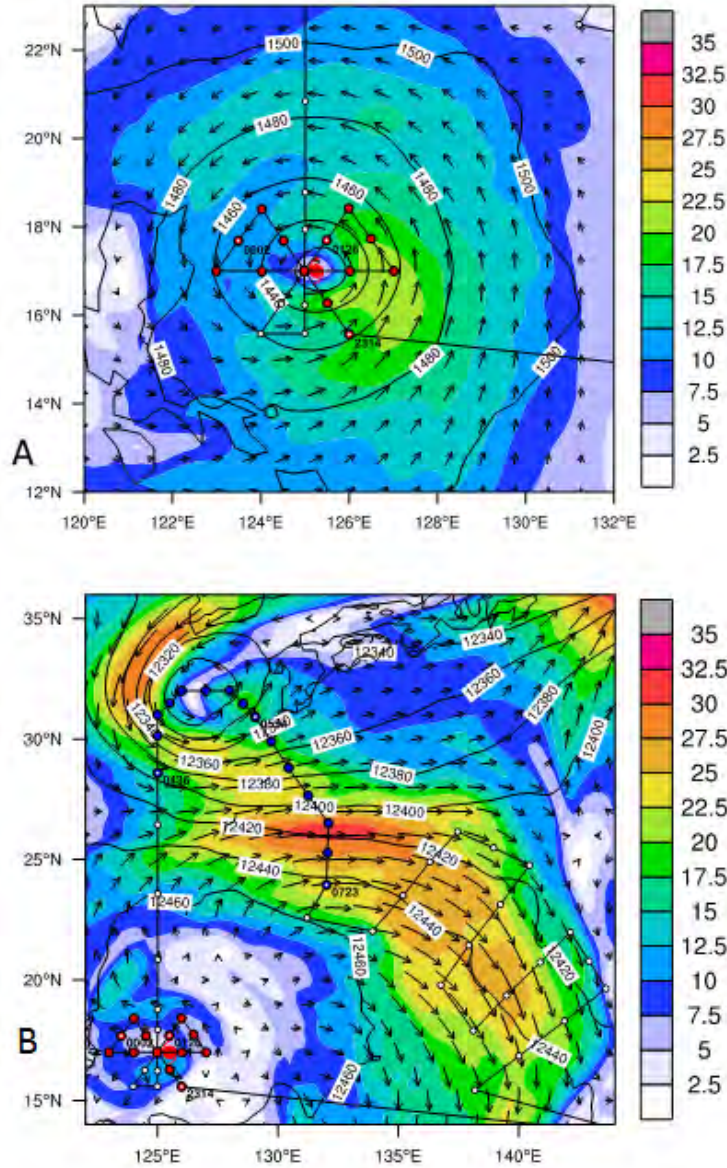


Figure 8. Wind speed (m s^{-1} , shading and vectors) and geopotential height (m, contours) from the ECMWF analysis at (A) 850 hPa and (B) 200 hPa. Panel (A) is valid at 0000 UTC 9 September 2008, and panel (B) is valid at 0600 UTC 9 September 2008. The black line indicates the pseudo-flight track used to derive the pseudo-dropwindsonde observations (white and color-filled circles along the flight track) from the ECMWF analysis. The red-filled dropwindsonde locations in panel (A) indicate the inner-core pseudo-dropwindsondes assimilated at 0000 UTC 9 September, while the blue-filled dropwindsonde locations in panel (B) indicate the environmental pseudo-dropwindsondes assimilated at 0600 UTC 9 September. The starting, middle, and ending times (UTC) are indicated for each pseudo-dropwindsonde set.

THIS PAGE INTENTIONALLY LEFT BLANK

III. BACKGROUND

A. EVOLUTION OF SINLAKU

Typhoon Sinlaku was one of four typhoons to be observed during the T-PARC experiment. At 1800 UTC 8 September 2008, Sinlaku formed just west of Luzon Island in the Philippines (Figure 9). The T-PARC focus was split into two periods during the lifetime of Sinlaku. A series of aircraft missions were conducted beginning on 9 September 2008 (Chou et al. 2011) as Sinlaku moved northward toward recurvature over the northern portion of Taiwan. Several missions were then conducted following recurvature when Sinlaku moved into the midlatitude and underwent extratropical transition (Sanabia 2010).

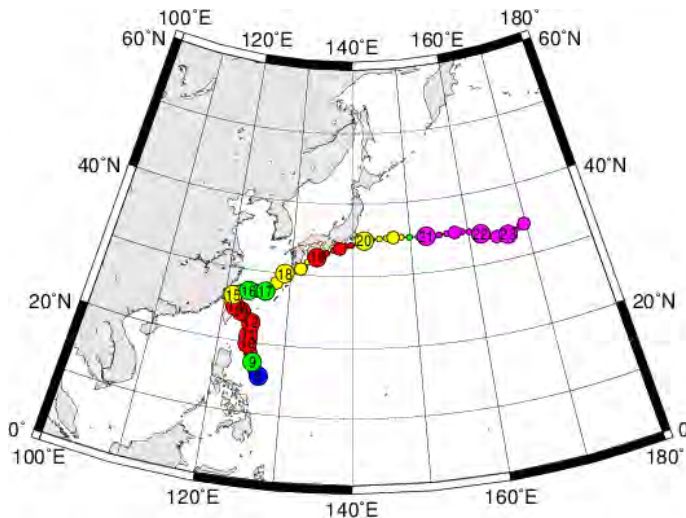


Figure 9. The track of TY Sinlaku depicted by intensity such that blue is a tropical disturbance, green is a tropical depression, yellow is a tropical storm, red is a typhoon, and magenta is an extratropical cyclone. The numbers in each circle define the day in September 2008. (From Kitamoto National Institute of Informatics (NII))

At 1430 UTC on September 7 2008, JTWC issued a classification of “poor” for an area of interest near 16.3N 128.5E in the Philippine Sea due to persistent convective activity (JTWC, 2008). Infrared satellite imagery (Figure 10) indicated flaring deep

convection associated with a developing low-level circulation center (LLCC). At this time, the indicated wind speed from the advanced scatterometer (ASCAT) ranged between 15 and 20 kt (not shown). The LLCC was developing beneath a broad upper-level anticyclone. Vertical wind shear was low, while a moderate level of upper level diffluence existed. The minimum sea level pressure (SLP) was estimated to be near 1006 hPa with winds estimated to be between 12 and 18 kt.

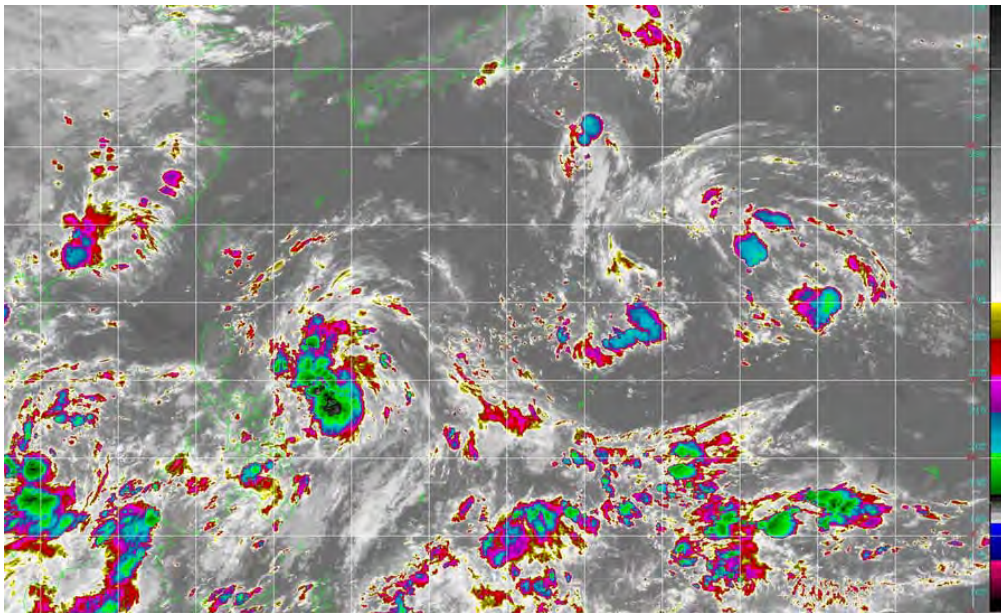


Figure 10. Enhanced infrared satellite imagery from MTSAT2 at 1430 UTC 7 September 2008. The black arrow points to an area of deep convection associated with the pre-Sinlaku disturbance. (From T-PARC Catalog)

At 2200 UTC 7 September 2008, JTWC upgraded the classification to “fair” for cyclone development over the next 24 hours due to “favorable upper level conditions despite minimal low level organization.” Water vapor imagery indicated building deep convection over a weak LLCC (Figure 11). The strong upper-level outflow on the poleward edge of the convective disturbance was enhanced by an upper-level cyclonic circulation that was directly to the east of the pre-Sinlaku disturbance. At this time, JTWC estimated maximum surface level winds to be 15 to 20 kt, with a SLP near 1005 hPa.

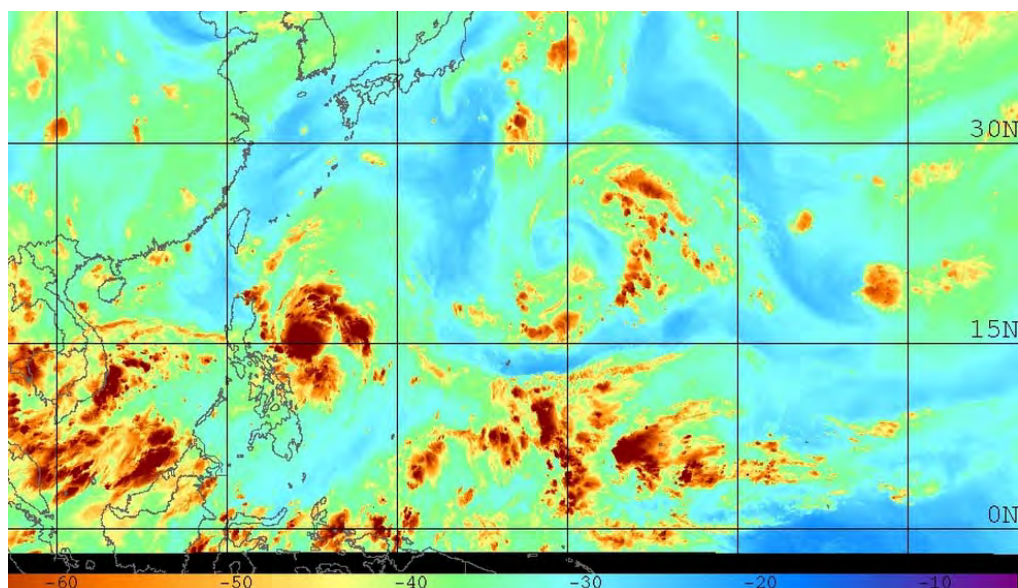


Figure 11. Water vapor imagery MTSAT at 2157 UTC 9 September, 2008 showing area of deep convection. (From T-PARC Catalog)

At 0600 UTC on 8 September 2008, a tropical cyclone formation area (TCFA) alert was issued by JTWC. Deep convection continued to grow near a consolidating LLCC. An upper level anticyclonic circulation along with low vertical wind shear and conditions favorable for upper level diffluence above the disturbance area were all favorable for continued development of the convective disturbance. The upper-level cyclonic cell to the east continued to influence the outflow on the poleward side of the circulation. Surface winds had increased to near 23 kt as the SLP continued to fall to 1004 hPa. JTWC forecasters upgraded the potential for a significant TC to occur within the following 24 hours to “good.”

The first warning was issued at 1500 UTC 8 September for tropical depression 15W. Sustained winds had reached 30 kt with gusts of 40 kt. The consolidation of deep convection at the storm center became clear in infrared imagery taken at 1430 UTC 8 September (Figure 12). Deep convective cloud bands were seen wrapping into the LLCC.

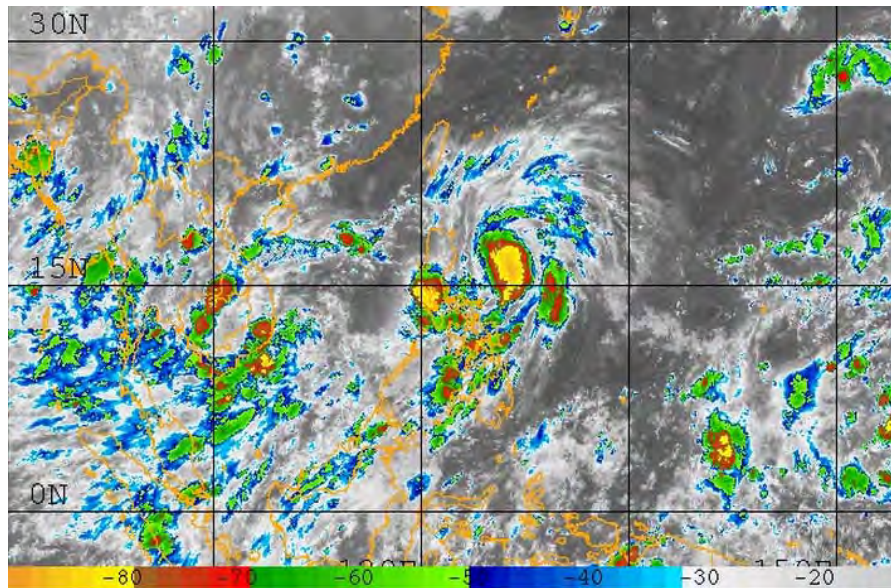


Figure 12. Enhanced infrared satellite imagery from MTSAT 2 at 1430 UTC 8 September 2008. (From T-PARC Catalog)

A period of rapid intensification began on 9 September 2008. Over the previous period, SLP dropped to 986 hPa, and surface winds increased to 55–60 kt. The center of vorticity was situated beneath a well-defined area of upper-level divergence. By 2032 UTC 9 September, a WC-130J flight reported a SLP of 938 hPa and a maximum surface wind of 82 kt as measured by the SFMR. A central dense overcast (CDO) was becoming better defined with intermittent eye wall development as seen in visual and IR imagery (not shown). The outflow jet was primarily oriented toward the northeast quadrant of the storm. The development of Sinlaku from 7–9 September is well depicted in IR imagery (Figure 13).

By 10 September, a well-defined eye was visible as Sinlaku reached maximum intensity with a SLP of 927 hPa and maximum winds estimated near 120 kt (Figure 14). In satellite imagery there is evidence of dry continental air to the north and west of the storm (Figure 13). While these conditions would suggested some weakening of the storm, the storm track was moving slowly in a northerly direction over a region of high ocean heat content (OHC) (Figure 15), which may have contributed to maintenance of the strong intensity. By this time, the previous prediction of the storm to recurve had been

reassessed due to the weakening subtropical steering ridge resulting in a continued drift toward Taiwan.

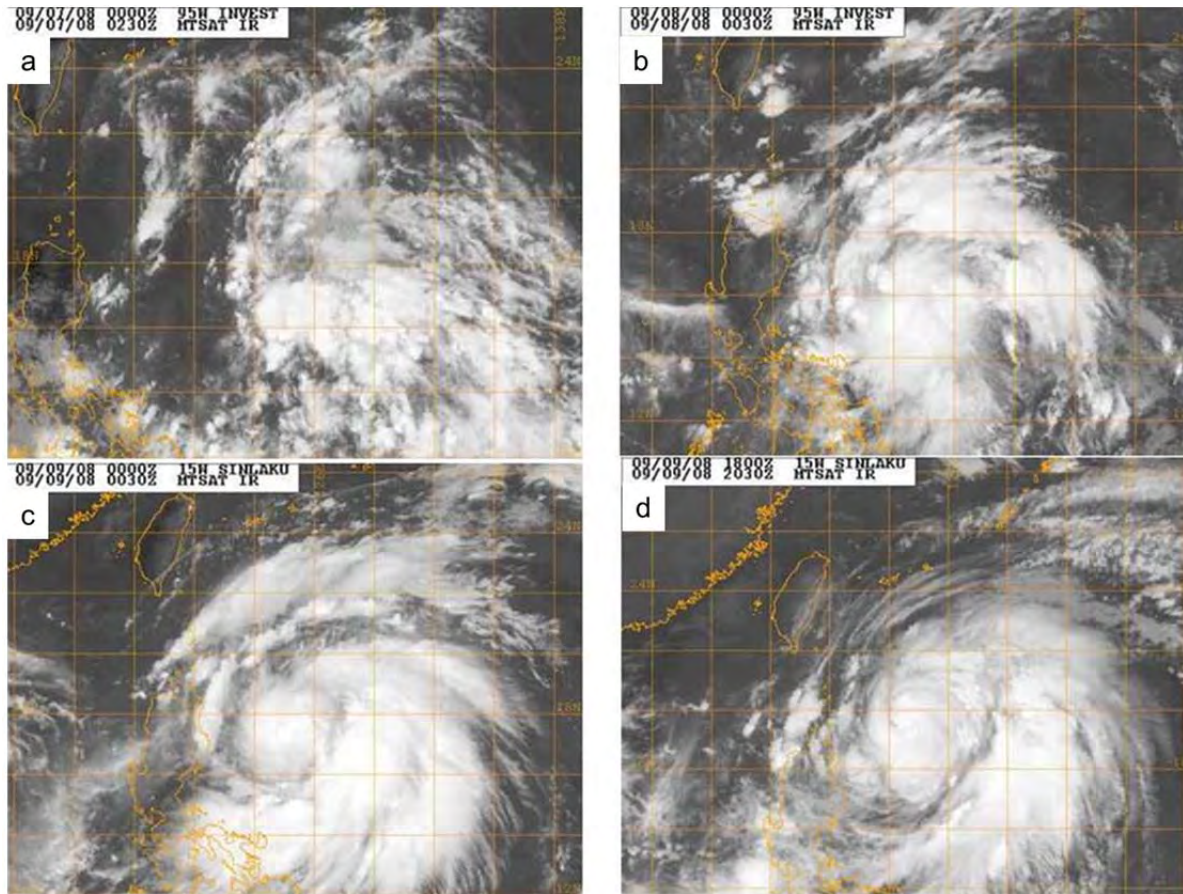


Figure 13. Infrared imagery from MTSAT 2 at (a) 0230 UTC 7 September; (b) 0032 UTC 8 September ; (c) 0030 UTC 9 September; and (d) 2030 UTC 9 September. (From T-PARC Catalog)

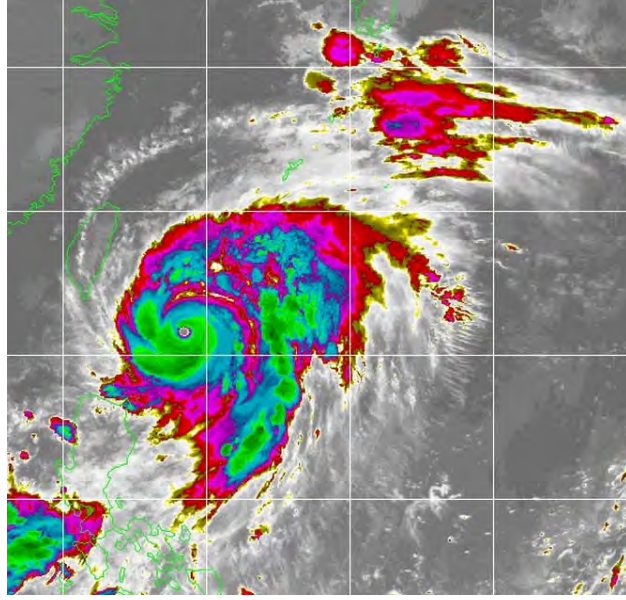


Figure 14. Infrared imagery from MTSAT2 at 1730 UTC 10 September (from T-PARC Catalog).

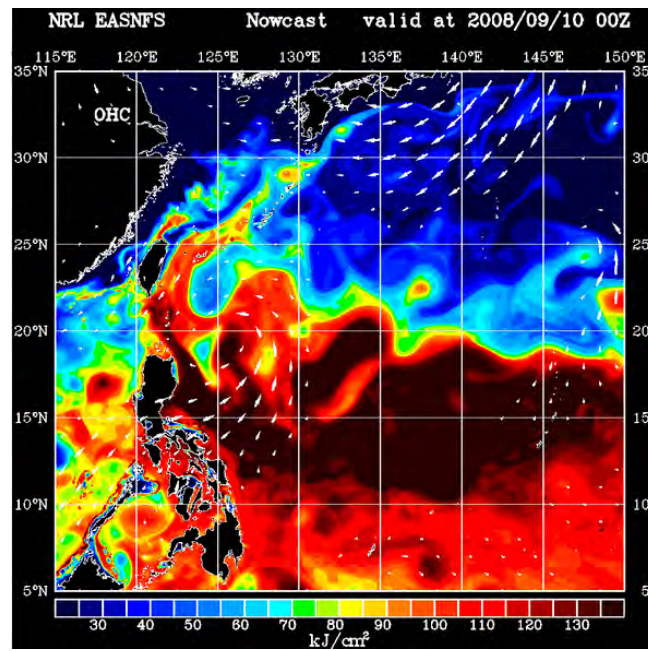


Figure 15. Analyzed OHC (kJ cm^{-2}) valid 0000 UTC 10 September 2008. Circle represents the location of the storm (from the East Asian Seas Nowcast Forecast System (EASNFS)).

An eyewall replacement cycle began near 1750 UTC 10 September (Figure 16a) and proceeded over the next 17 h to 1135 UTC 11 September (Figures 16b–d). The eyewall replacement cycle coincided with some weakening in storm intensity. Also the storm moved over a region of decreased OHC, which may have also contributed to the decrease in storm intensity at this time (Figure 17).

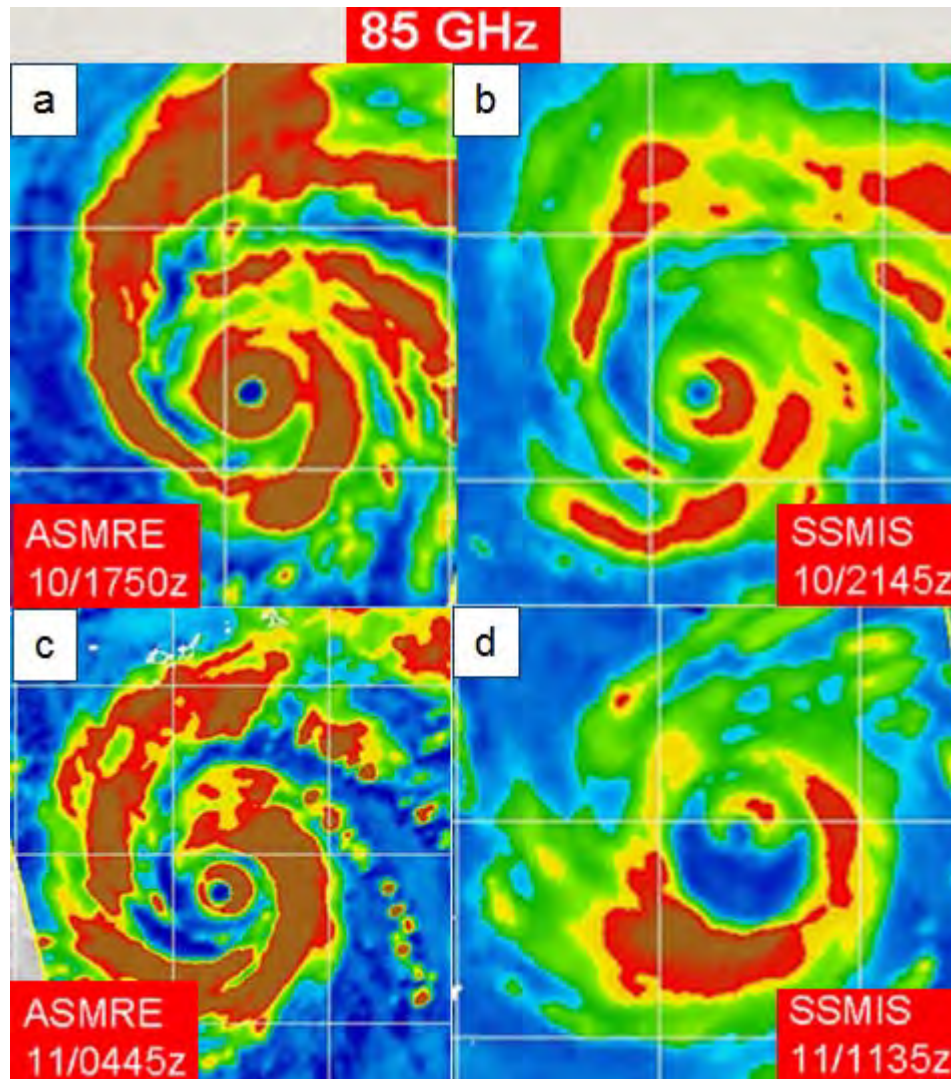


Figure 16. Eyewall replacement between 10 and 11 Sept 08 (after TPARC_2008 weather summary)

Over the next 24 hours, Sinlaku tracked to the northwest and continued to weaken. The weakening was likely due to increased vertical wind shear (not shown) and

movement over a region of reduced OHC (Figure 17). At 1750 UTC 12 September, aircraft missions deploying dropsondes reported maximum surface winds of 98 kt and SLP of 954 hPa.

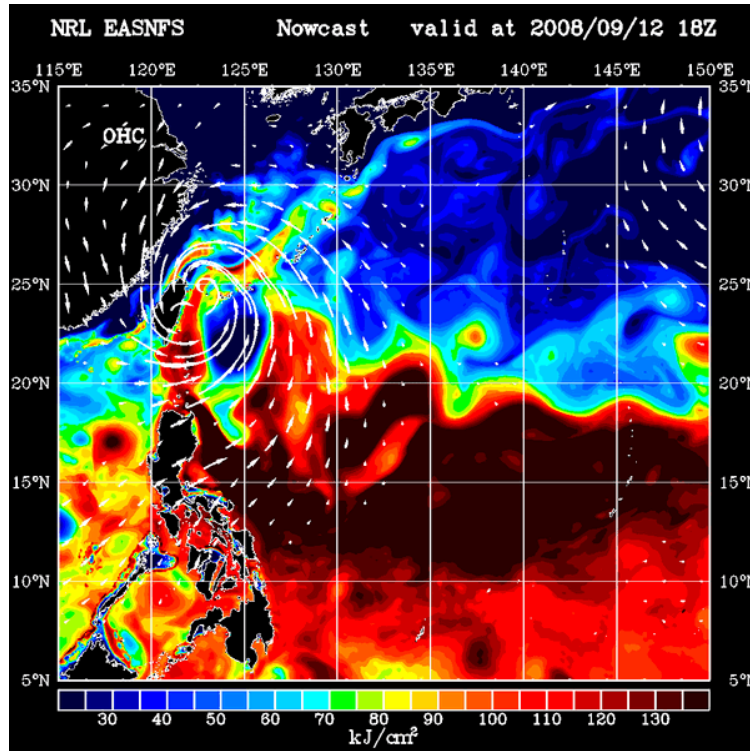


Figure 17. Analyzed OHC (kJ cm^{-2}) valid 1800 UTC 12 September 2008 (from T-PARC Catalog and Naval Research Lab East Asian Seas Nowcast / Forecast System (NRL EASNFS)).

As Sinlaku approached Taiwan during 12-13 Sept, the eyewall contracted, which is clearly identified in microwave imagery (Figure 18). At this time, the satellite-based intensity estimate was 102 kts vertical wind shear increased (not shown) and Sinlaku made landfall on 13 September. Reported observations from the Yonaginijima Island (eye did not pass directly over the island) reported maximum winds near 92 kt and SLP of 962 hPa (Figure 19).

Over the ensuing days, Sinlaku continued to weaken and moved slowly to the NW before recurvature on 14 September. Comparison of IR imagery comparisons from 13-14 Sept showed considerable decreased intensity.

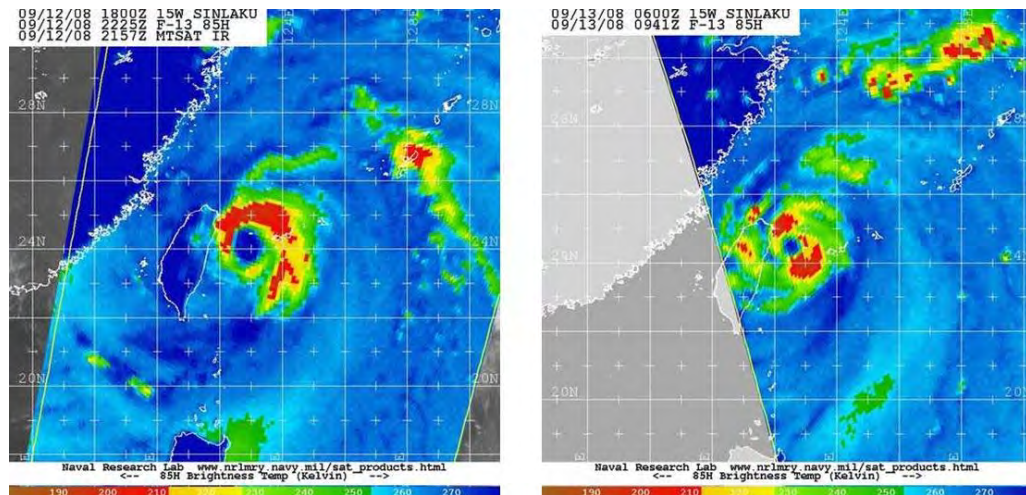


Figure 18. Combined 85 GHz microwave and infrared imagery at (a) 2157 UTC 12 September and (b) 0941 UTC 13 September (from Naval Research).

13 September 2008 Yonaginijima

Latitude: 24°28.0'N, Longitude: 123°0.6'E, Altitude: 30m [Today](#) [High/Low](#)

No

Time	Temperature	Precipitation	Wind Direction	Wind Speed	Sunshine Duration	Humidity	Pressure
Hour	°C	mm	In 16 Compass Points	m/s	h	%	hPa
1	25.2	10.5	NE	38		95	975.5
2	25.1	30.5	NE	34		96	974.9
3	25.2	23.5	NE	35		96	974.0
4	25.8	16.0	NE	32	0.0	96	973.7
5	25.8	9.5	NE	40	0.0	96	964.4
6	24.5	17.5	ENE	43	0.0	97	962.5
7	25.5	13.0	E	33	0.0	98	962.4
8	25.4	8.5	E	35	0.0	97	967.6
9	25.6	6.5	E	32	0.0	97	963.2
10	24.7	8.5	ESE	33	0.0	97	965.7
11	25.2	59.0	ESE	37	0.0	98	968.1
12	25.3	86.0	SE	42	0.0	98	966.2
13	25.4	42.5	SE	40	0.0	100	968.1
14	25.3	59.5	SE	38	0.0	100	972.9
15	25.8	53.5	SE	29	0.0	100	975.7
16	25.5	76.0	SE	38	0.0	100	971.7
17	25.7	79.0	SE	33	0.0	100	973.9
18	25.8	78.0	SE	33	0.0	100	974.4
19	26.1	56.5	SE	33	0.0	100	976.9

Figure 19. Observations from Yonaginijima Airport 13 Sep 08 (from TPARC_2008 weather summary)

After passing by Taiwan and recurving, Sinlaku nearly became stationary for a period of 48 hours. By 18 September, another period of rapid intensification occurred as winds increased by 20 knots over an 18-h period and Sinlaku regained typhoon intensity. Finally on 20 September, 2008, a final warning was issued on Sinlaku as it moved east of Tokyo, Japan. During the lifecycle of Sinlaku, 47 warnings were issued by JTWC, and the max sustained winds topped out at 125 knots.

B. SYNOPTIC ANALYSIS DURING SINLAKU

The synoptic environment of the pre-recurvature period of Sinlaku is defined using the National Centers for Environmental Prediction (NCEP) Climate Forecast System Reanalysis (CFSR) (Saha et al. 2010). The NCEP CFSR has 38 km global resolution and fields available every 6 h. The primary synoptic factors relevant to the movement of Sinlaku are identified for eventual comparison among the experimental forecast fields initialized using varying data sources.

The synoptic analysis identifies the basic large-scale features over the western North Pacific that influenced the motion of Sinlaku during this period of high forecast uncertainty. The role of the low-level monsoon trough and subtropical ridge is examined. The role of a midlatitude trough is also examined in relation to upper-level outflow patterns and the influence on recurvature.

1. Sea Level Pressure

During the transition season in the western north Pacific the low-level atmosphere can be generally characterized as a near equatorial monsoon trough that extends from the west to the Philippines with temporary eastward extension over the Philippine Sea. Convection often forms in the monsoon trough and contributes large-scale upper level mass divergence. At the eastern edge of the monsoon trough, easterly trade winds crossing the Pacific and meet the westerly winds associated with the equatorial portion of the monsoon trough. This defines a region of low-level confluence and convergence that contributes to the forcing of deep convection that may propagate westward along the monsoon trough axis. Just poleward of the monsoon trough, a strong subtropical ridge covers most of the subtropical western north Pacific. The strong easterly flow between

the poleward portion of the monsoon trough and the equatorward side of the subtropical ridge provide a general steering flow in which most TCs that form in the trough move northwestward. If the subtropical ridge is weakened by the influence of a midlatitude trough, the general easterly steering flow weakens and a TC may become influence by the westerly midlatitude flow and recurve into the midlatitudes.

Sinlaku formed within the low-level trough associated with the western North Pacific summer monsoon (WNPSM). Throughout the 2008 summer, WNPSM was weak as trade winds dominated the region of the Philippine Sea. Enhanced areas of active monsoonal flow during the onset of Sinlaku in early September 2008 had the effect of increased convective activity, clouds and precipitation. On 1200 UTC 9 September, the low pressure center for Sinlaku was situated within the WNPSM just east of Luzon, Philippines (Figure 20). A weak low pressure system to the northeast of Sinlaku was a low-level reflection of an upper-level trough. The combination of the Sinlaku disturbance and the low pressure to the northeast contributed to a weakened subtropical ridge and the slow northward movement of Sinlaku.

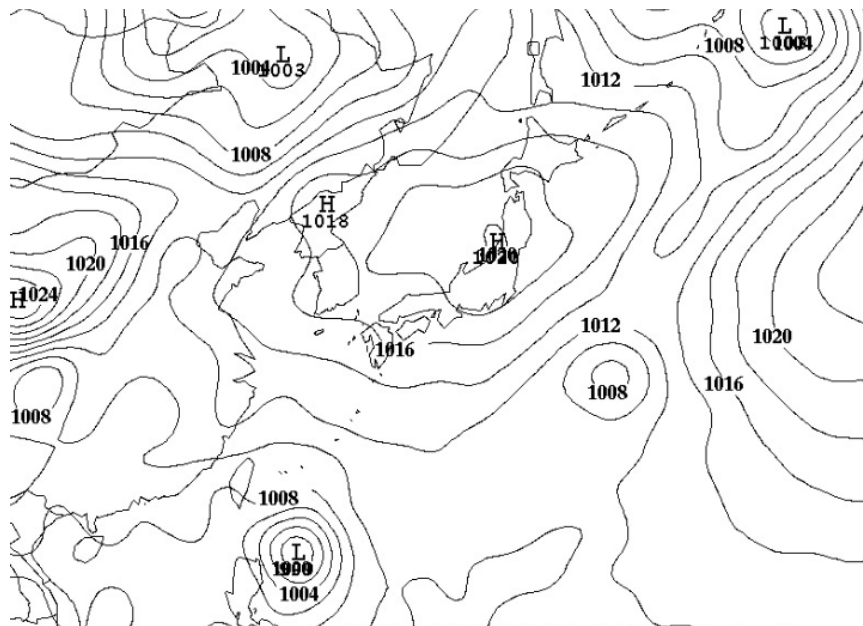


Figure 20. Analyzed mean sea level pressure (contours in 2 hPa increments) for 1200 UTC 9 September 2008

2. 850 hPa

The subtropical ridge was pushed farther poleward than normal due to the orientation of the monsoon trough to the northeast from Sinlaku to the low pressure over the subtropics northeast of Sinlaku (Figure 21). These low pressure systems forced the western extension of the subtropical ridge to be over Japan.

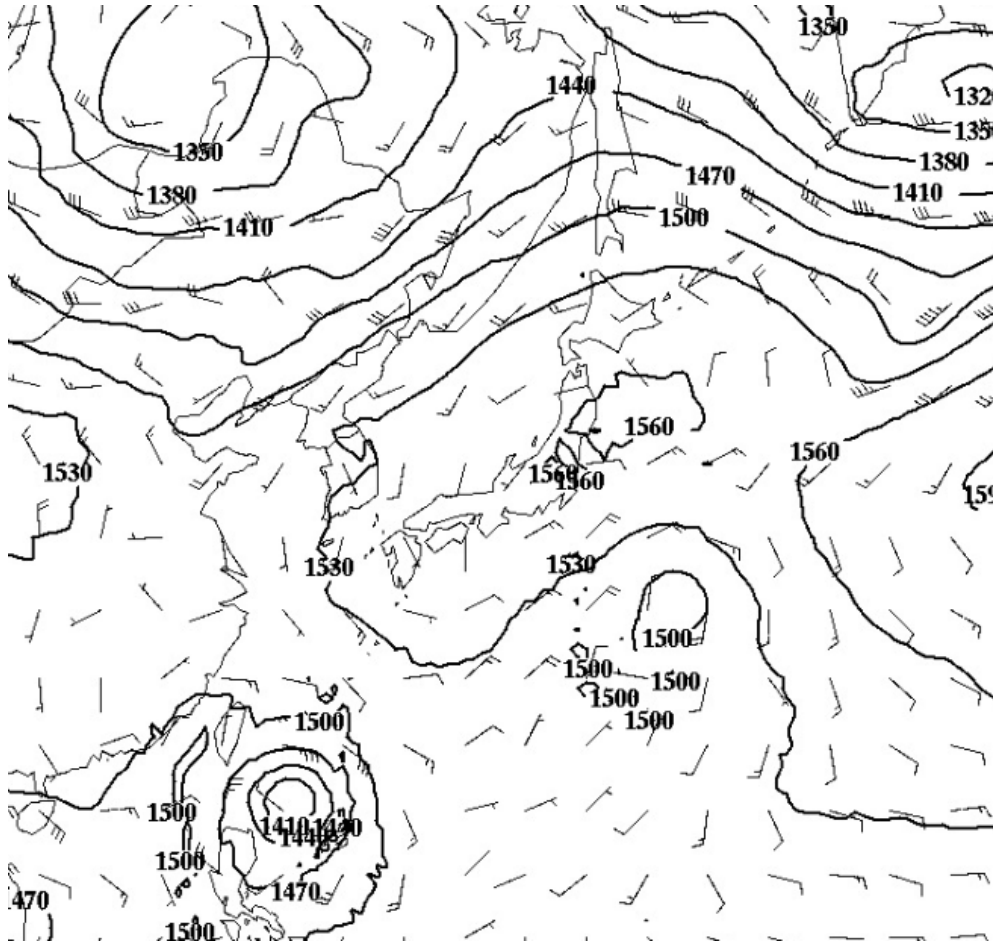


Figure 21. Analyzed 850 hPa winds (m s^{-1}) and geopotential height (contours, in 30 m intervals) for 1200 UTC 9 September 2008

The forcing of the subtropical ridge to the north, reduced the easterly steering flow over the environment of Sinlaku and resulted in the slow northward movement of the TC during this time period.

3. 500 hPa

An upper-level midlatitude trough was moving off of eastern China and began to erode the subtropical (figure 22). As Sinlaku became more mature and moved northwest, its speed of advance was too slow and Sinlaku was not caught up by steering to the east due to the long wave trough to the north. This would have presumably caused Sinlaku to recurve sooner. Consequently, the turn of Sinlaku to the north and eventual northeast was delayed until after landfall over northern Taiwan.

4. 200 hPa

At 200 hPa, the outflow from Sinlaku was turned sharply to the east and equatorward. The turning of the outflow was due to the influence of the upstream midlatitude trough. The resulting strong confluent westerly flow at 200 hPa was immediately poleward of the storm (Figure 22).

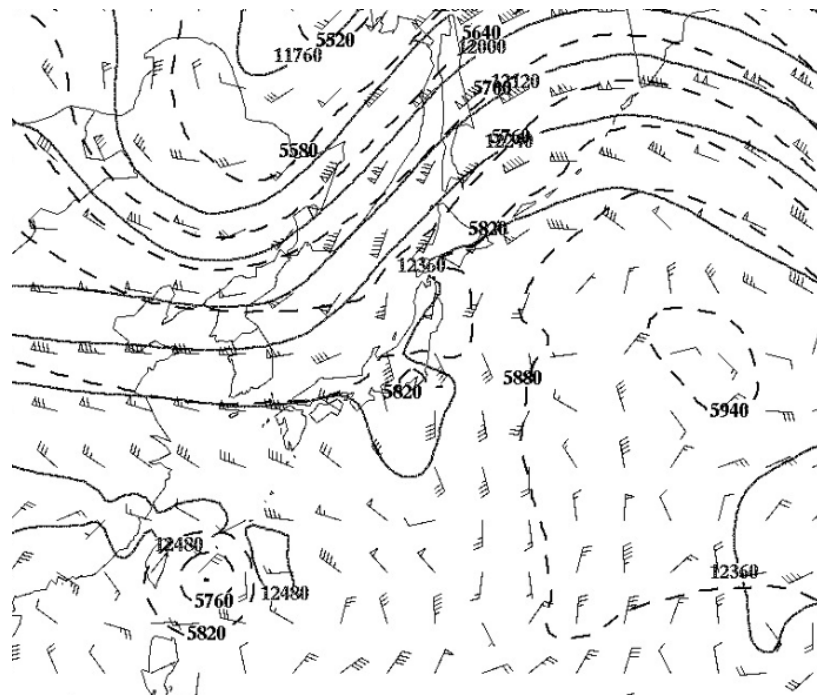


Figure 22. Analyzed mean sea level pressure at 1200 UTC 9 September 2008. Dashed and solid lines represent 500 hPa and 200 hPa geopotential heights (m), respectively. Wind barbs are at 200 hPa with small barbs representing 5 m s^{-1} .

THIS PAGE INTENTIONALLY LEFT BLANK

IV. OBSERVATION SENSITIVITY EXPERIMENTS

A. DETERMINISTIC WRF MODEL (WRF-OPS) SIMULATIONS

The initial and lateral boundary conditions for the WRF deterministic forecast WRF-OPS and the WRF ensemble forecasts were derived from the ECMWF operational forecast initialized at 1200 UTC 8 September 2008. To simulate real-time operations, the experimental model forecasts utilized the ECMWF forecast (labeled ECMWF-YOTC) for 1200 UTC 8 September to define the WRF-OPS single, deterministic model forecast. No data assimilation was conducted in the production of the WRF-OPS forecast. This allowed for comparison with the experimental runs to follow: WRF-CONV, WRF-C130, and WRF-PSEUDO, which all included data assimilation.

The forecast track and intensity forecast of WRF-OPS were compared with the JTWC best track data (Figure 23). In the WRF-OPS forecasts, Sinlaku made landfall on the southern end of Taiwan whereas the actual storm crossed the very northern portion of Taiwan. In contrast, the WRF-ANAL forecast was more in agreement with JTWC best track (Figure 23), as expected. The striking departure of WRF-OPS from the best track and WRF-ANAL suggests a cumulative positive effect of observations on TC forecasts. The forecast intensity from WRF-ANAL and WRF-OPS (Figure 24) matched the JTWC best track intensity except near 11 and 12 September. At this time in WRF-OPS forecasts, Sinlaku was overland in southern Taiwan so the mean sea-level pressure (MSLP) increased rapidly (Figure 24). Both WRF intensity forecasts are much more accurate than the operational ECMWF forecasts or the analyzed ECMWF intensities.

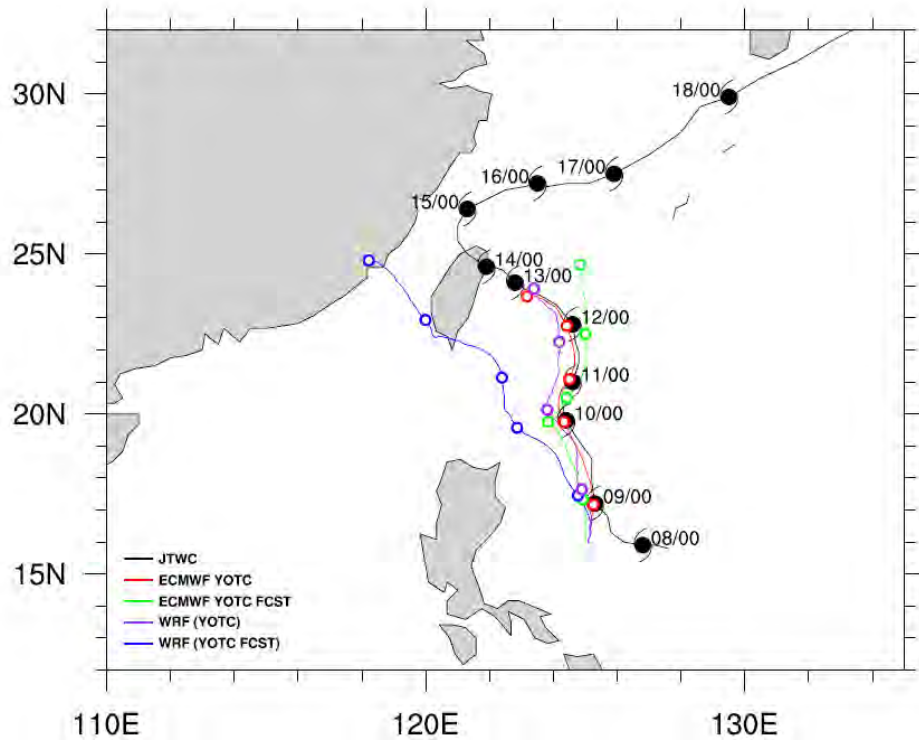


Figure 23. Sinlaku track comparison where the black, red, green, purple, and blue tracks represent JTWC best track, ECMWF YOTC analysis, ECMWF YOTC forecast, WRF (YOTC) analysis, and WRF-(YOTC forecast), respectively.

During this period, JTWC forecast Sinlaku to recurve to the east much sooner than it actually did. The JTWC warning number four initialized at 0600 UTC on 9 September forecasted a 304 nm closest point of approach (CPA) for Taipei (Figure 25). Just 48 hours later, CPA to Taipei was reduced to 92 nm (Figure 26). By 14 September the eye of Sinlaku was passing over Taipei (not shown). The uncertainty of the forecast was well represented by the large area of possible track locations defined in relation to each forecast (shaded region in Figures 25 and 26).

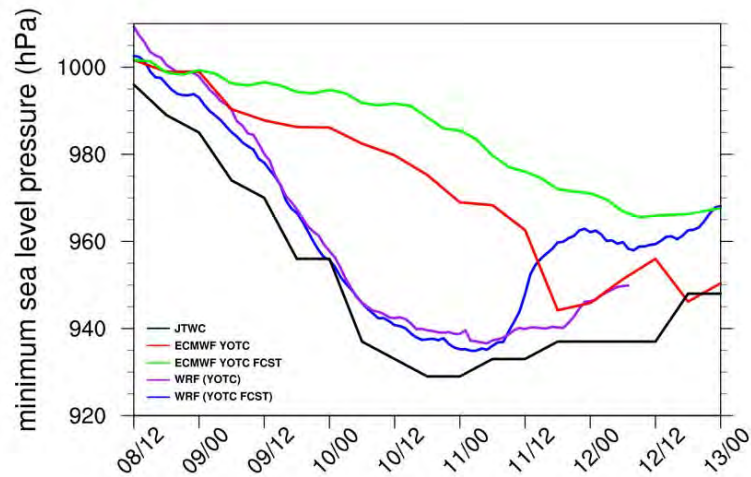


Figure 24. Sinlaku intensity comparison where the black, red, green, purple, and blue lines represent JTWC best track, ECMWF YOTC analysis, ECMWF YOTC forecast, WRF-ANAL and WRF-OPS, respectively.

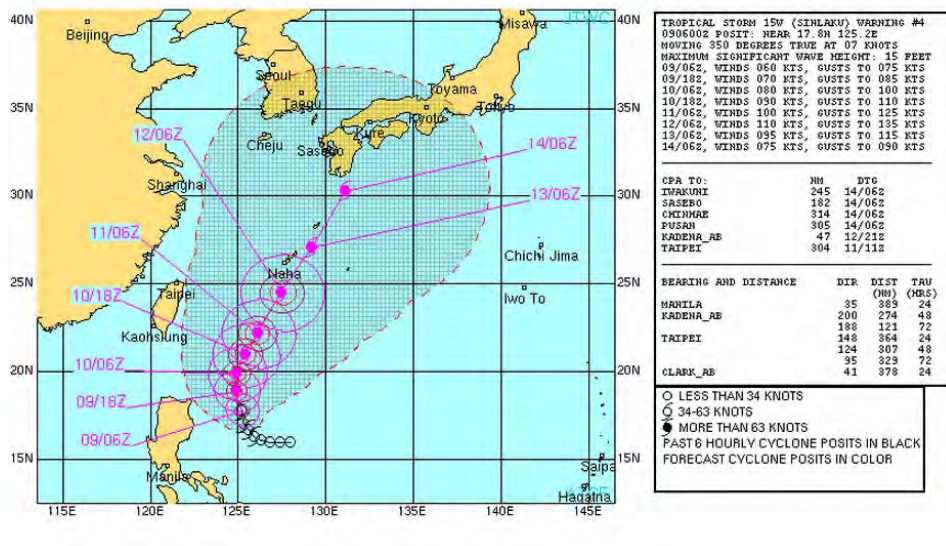


Figure 25. JTWC TC warning number 4 from 0600 UTC 9 September 2008 (from JTWC).

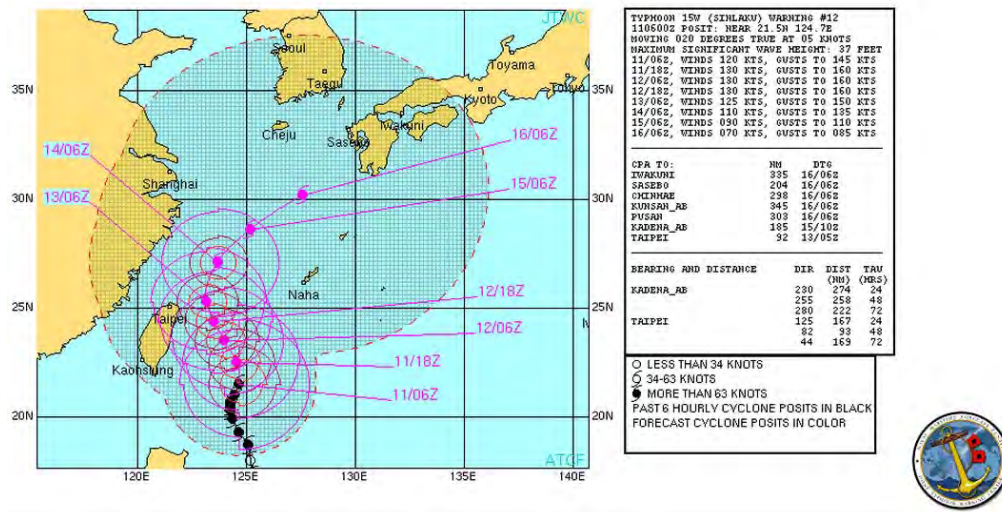


Figure 26. JTWC TC warning number 12 from 0600 UTC 11 September 2008 (from JTWC).

The WRF-OPS forecast verifying at 1200 UTC 8 September (Figure 27) had a fairly weak ridge at 850 hPa north and east of Sinlaku. This is defined by the red 1530 m contour in Figure 27. A well-established monsoon trough extended from the storm center to the southwest (yellow contour in Figure 28). A stronger ridge existed at 500 hPa, which is defined by the red contour in Figure 28. The most prominent upper level feature at 200 hPa (Figure 29) is the outflow that extends north of the storm. The confluence of the outflow and the eastward-moving trough leads to strong westerly flow north of Sinlaku (Figure 29).

In the 12 h forecast (Figure 30) verifying at 0000 UTC 9 September, the 850 hPa ridge strengthened and pushed farther south toward Sinlaku. The storm intensified and the monsoon flow that encompassed the TC had intensified. As the ridge strengthened, the storm moved more northwestward as defined by the red motion vector in Figure 30.

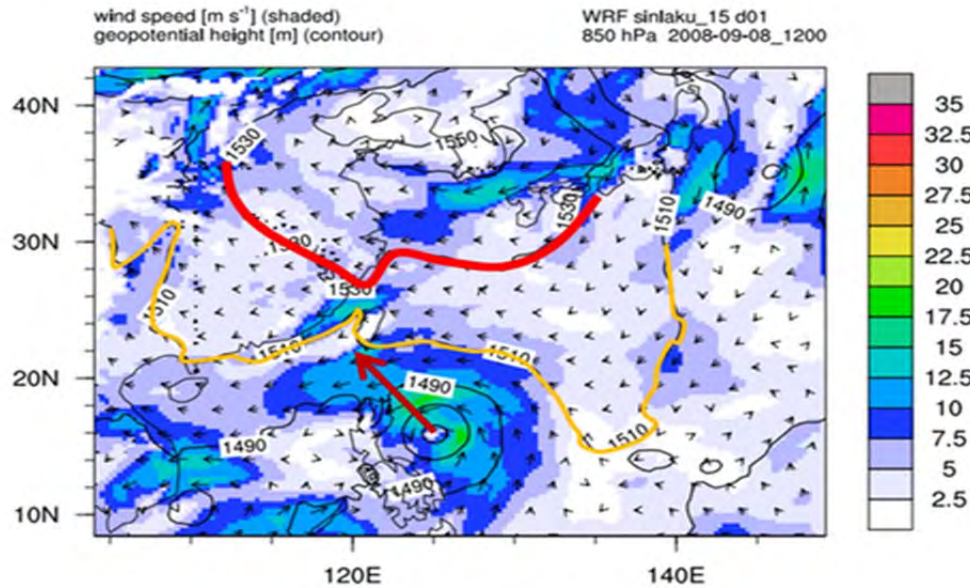


Figure 27. Analyzed winds (vectors) and speed (m s^{-1} , shaded) at 850 hPa and 850 hPa geopotential heights (m, contours at 20 m intervals). The red vector represents general storm motion. The red and yellow contours represent 1530 m and 1510 m geopotential heights,, respectively, at 1200 UTC 8 September.

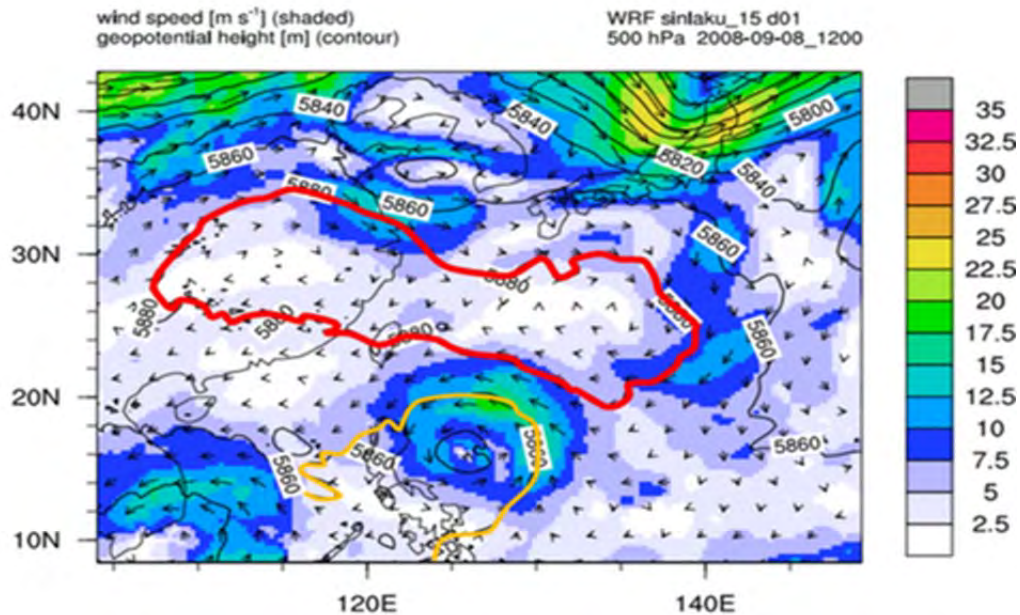


Figure 28. Analyzed winds (vectors) and speed (m s^{-1} , shaded) at 500 hPa and 500 hPa geopotential heights (m, contours at 20 m intervals) The red and yellow contours represent 5880 m and 5860 m geopotential heights,, respectively, at 1200 UTC 8 September.

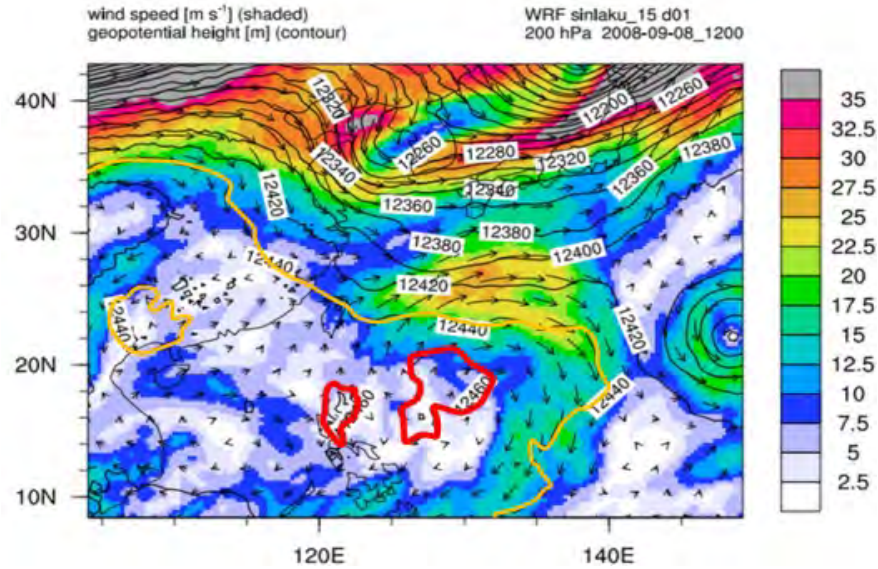


Figure 29. Analyzed winds (vectors) and speed (m s^{-1} , shaded) at 200 hPa and 200 hPa geopotential heights (m, contours at 20 m intervals). The red and yellow contours represent 12,460 m and 12,440 m geopotential heights, respectively, at 1200 UTC 8 September.

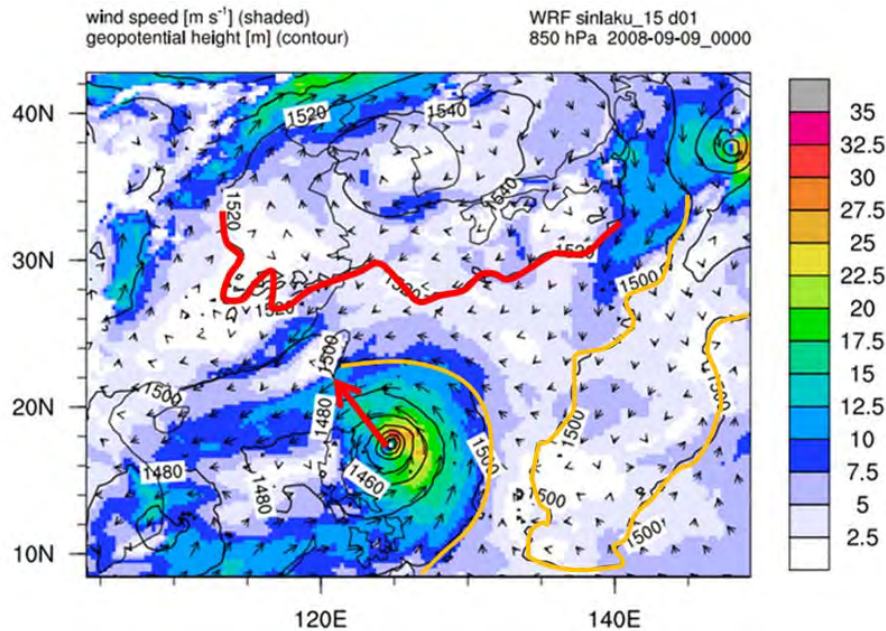


Figure 30. WRF-OPS 12-h forecast winds (vectors) and speed (m s^{-1} , shaded) at 850 hPa and 850 hPa geopotential heights (m, contours at 20 m intervals). The red vector represents general storm motion. The red and yellow contours represent 1520m and 1500 m geopotential heights, respectively, at 0000 UTC 9 September.

In the 18 h forecast that verifies at 0600 UTC on 09 September the surrounding environment of Sinlaku continued to change. The 850 hPa ridge (red 1520 m contour Figure 31) moved poleward. At 500 hPa the subtropical ridge defined by the red 5880 m contour in Figure 32 weakened north of Sinlaku was positioned just north of the storm. The ridge was no longer continuous north of the storm, which had begun to turn toward the north. At 200 hPa (Figure 33), the anticyclone over the TC expanded. To the north of the TC the midlatitude trough developed a closed circulation just southwest of Japan. The combination of the outflow and midlatitude trough contributed to a strengthening of the westerly flow (Figure 33) north of the storm.

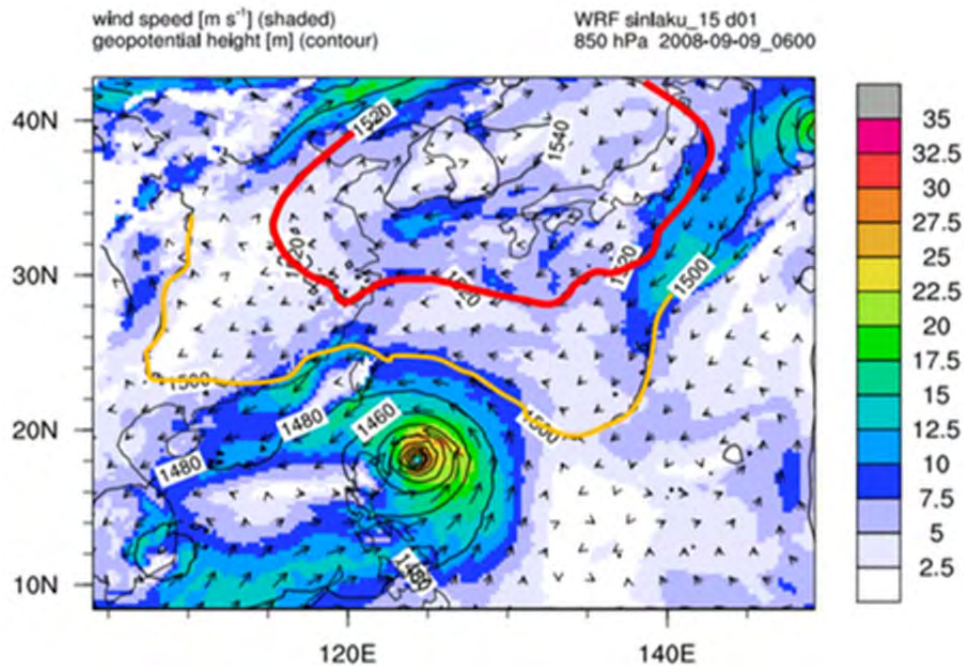


Figure 31. WRF-OPS 12-h forecast winds (vectors), and speed (m s^{-1} , shaded) at 850 hPa and 850 hPa geopotential heights (m, contours at 20 m intervals) The red and yellow contours represent 1520m and 1500 m geopotential heights, respectively, at 0600 UTC 9 September.

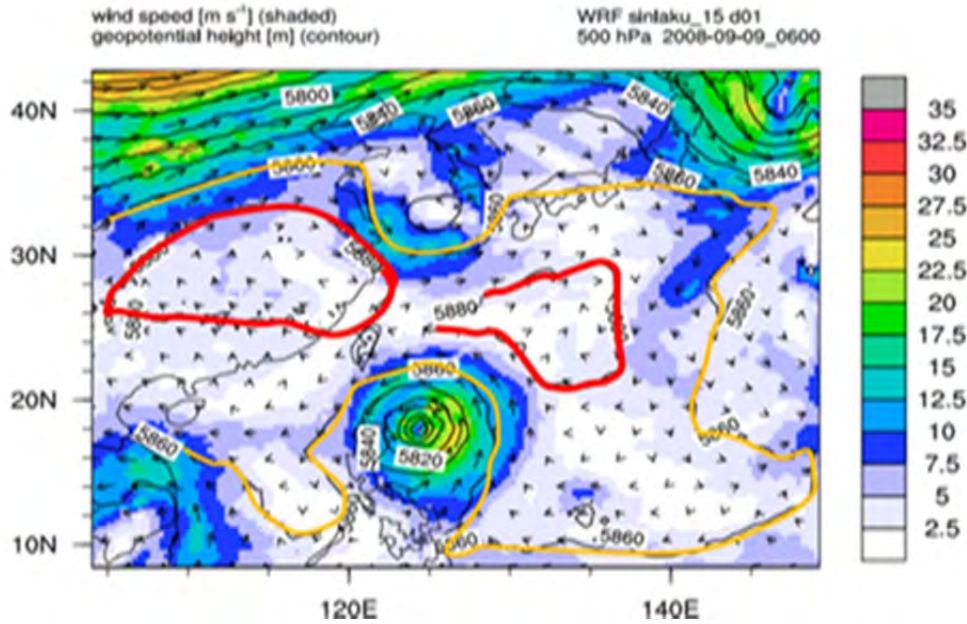


Figure 32. WRF-OPS 12-h forecast winds (vectors) and speed (m s^{-1} , shaded) at 500 hPa and 500 hPa geopotential heights (m, contours at 20 m intervals) The red and yellow contours represent 5880 m and 5860 m geopotential heights, respectively, at 0600 UTC 9 September.

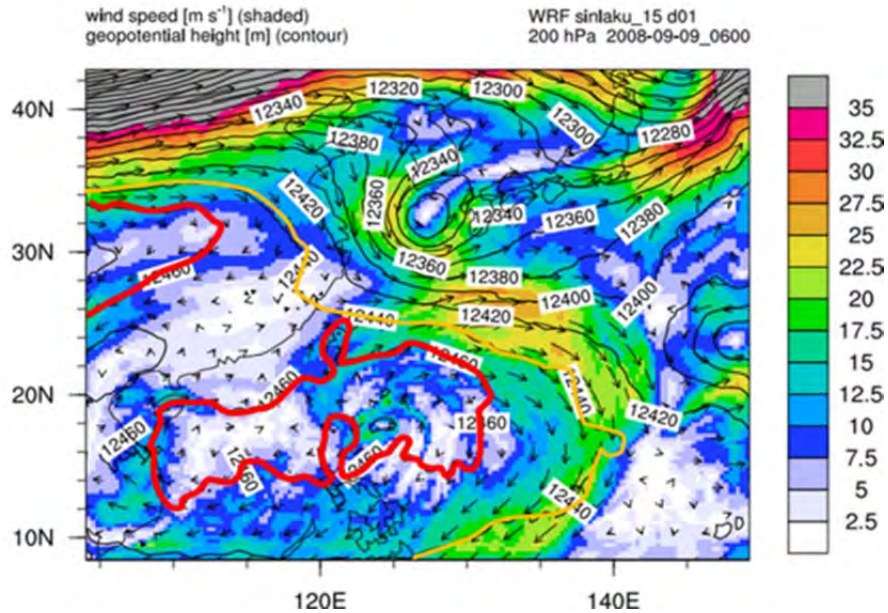


Figure 33. WRF-OPS 12-h forecast winds (vectors) and speed (m s^{-1} , shaded) at 200 hPa and 200 hPa geopotential heights (m, contours at 20 m intervals) The red and yellow contours represent 12,460 m and 12,440 m geopotential heights, respectively, at 0600 UTC 9 September.

At 1200 UTC on 9 September, the large-scale environment continued to evolve as Sinlaku tracked very slowly to the northwest. At 850 hPa (Figure 34), the western portion of the ridge to the north of the TC weakened. The weak mid-level ridge (red 5880 m contour in Figure 35) that previously stretched north of Sinlaku expanded over a larger area to the east of the storm (Figure 35). However, the ridge to the north of Sinlaku was still weak as the upper-level cyclone circulation evolved at 200 hPa at 0600 UTC (Figure 35) now extended down to 500 hPa. At 200 hPa level (Figure 36), the ridge over the storm intensified. The outflow from Sinlaku continued to merge with the digging and eastward-moving trough, which resulted in increased westerly winds to the north of the storm.

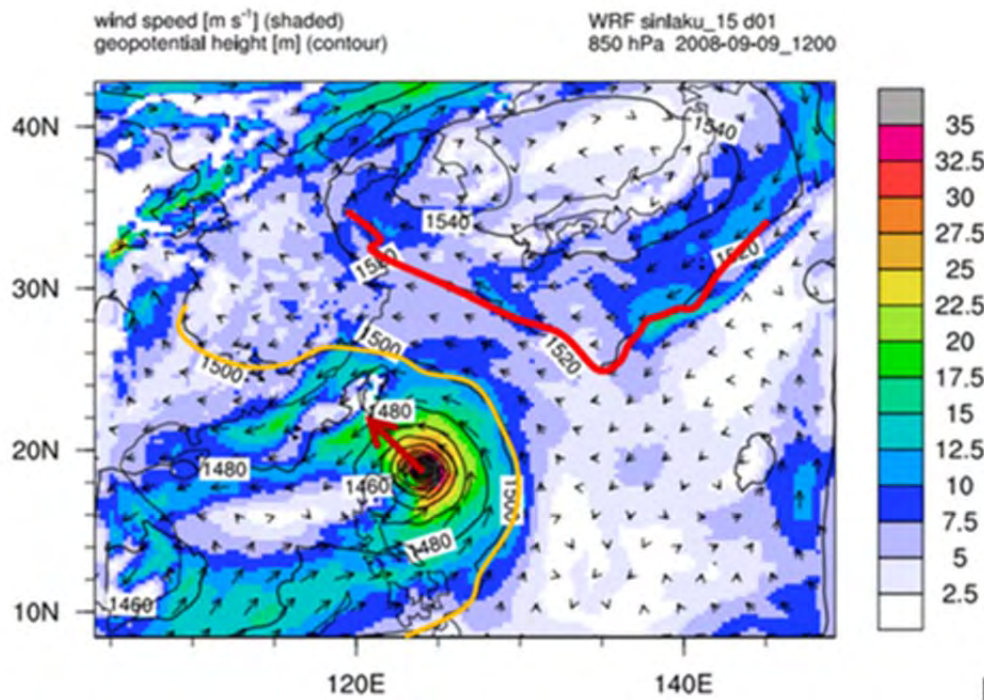


Figure 34. WRF-OPS 24-h forecast winds (vectors) and speed (m s^{-1} , shaded) at 850 hPa and 850 hPa geopotential heights (m, contours at 20 m intervals). The red vector indicates general storm motion. The red and yellow contours represent 1520 m and 1500 m geopotential heights, respectively, at 1200 UTC 9 September.

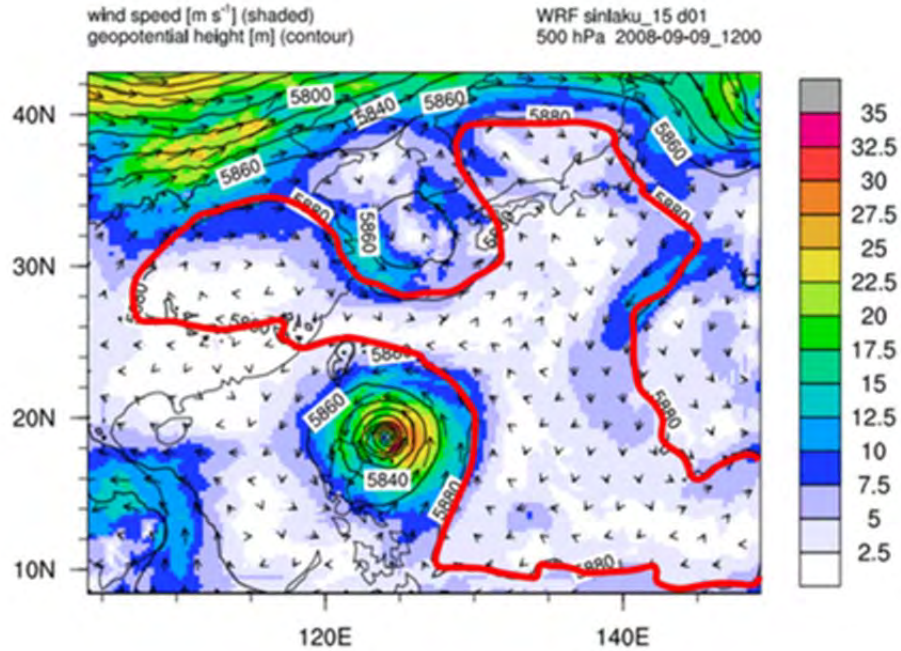


Figure 35. WRF-OPS 24-h forecast winds (vectors) and speed (m s^{-1} , shaded) at 500 hPa and 500 hPa geopotential heights (m, contours at 20 m intervals). The red contour represents 5880 geopotential heights at 1200 UTC 9 September

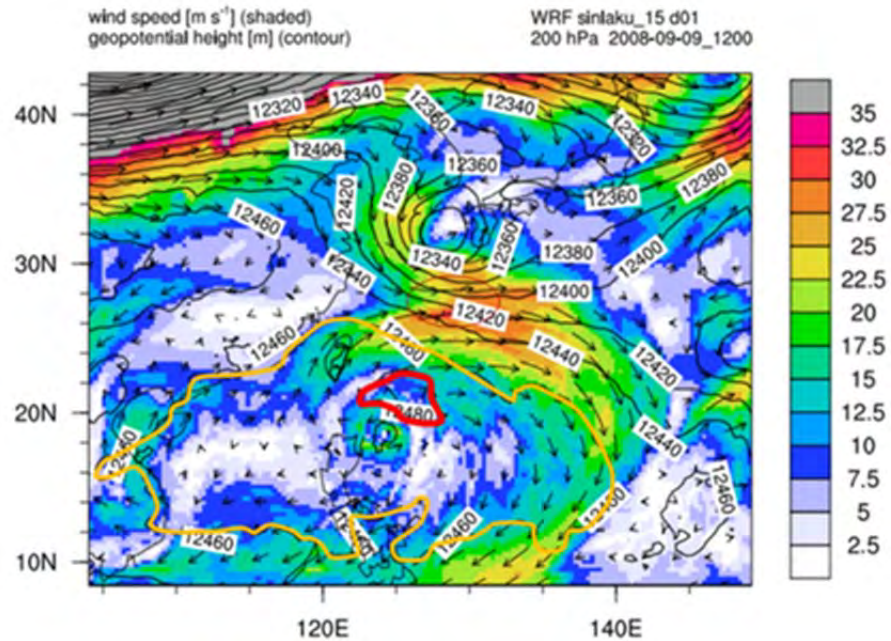


Figure 36. WRF-OPS 24-h forecast winds (vectors) and speed (m s^{-1} , shaded) at 200 hPa and 200 hPa geopotential heights (m, contours at 20 m intervals). The red and yellow contours represent 12,480 m and 12,460 m geopotential heights, respectively, at 1200 UTC 9 September.

In the 36 h forecast that verified at 0000 UTC 10 September (Figure 37), the low-level ridge (red 1530 contour in Figure 37) continued to weaken. The most dramatic change occurred at mid-levels (Figure 38) as the subtropical ridge north of the storm was replaced by the deepening midlatitude trough. However, the ridge did extend southward to be northeast of Sinlaku (Figure 38). The orientation was likely responsible for steering the storm more westward toward southern Taiwan. As the storm matured, the 200 hPa heights directly above the storm continued to increase (Figure 39). The outflow from Sinlaku continued to increase and wrap around to the east and south (Figure 39). The mid and lower level ridges continued to move east.

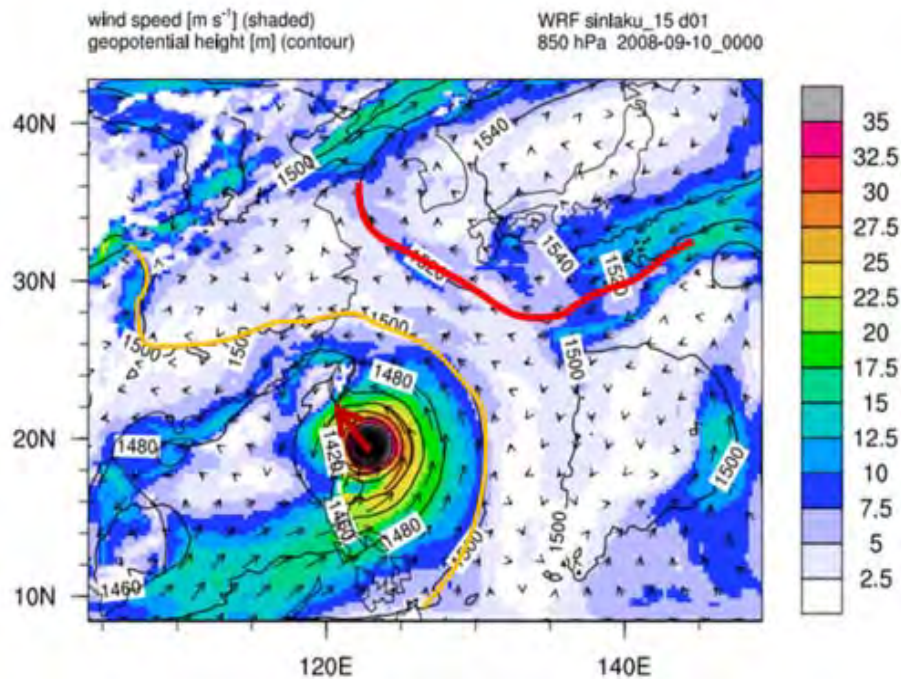


Figure 37. WRF-OPS 36-h forecast winds (vectors) and speed (m s^{-1} , shaded) at 850 hPa and 850 hPa geopotential heights (m, contours at 20 m intervals). The red vector indicates general storm motion. The red and yellow contours represent 1520 m and 1500 m geopotential heights, respectively, at 0000 UTC 10 September.

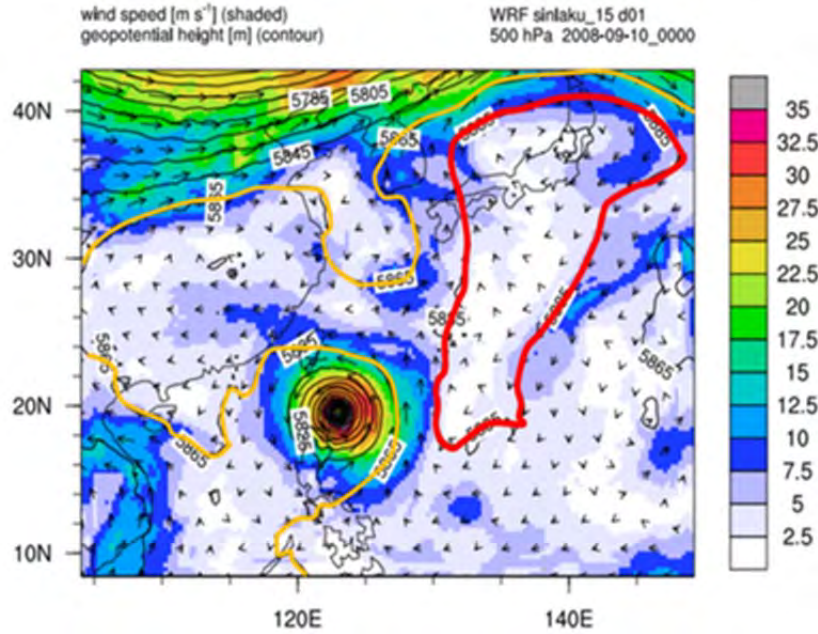


Figure 38. WRF-OPS 36-h forecast winds (vectors) and speed (m s^{-1} , shaded) at 500 hPa and 500 hPa geopotential heights (m, contours at 20 m intervals). The red and yellow contours represent 5885 m and 5865 m geopotential heights, respectively, at 0000 UTC 10 September.

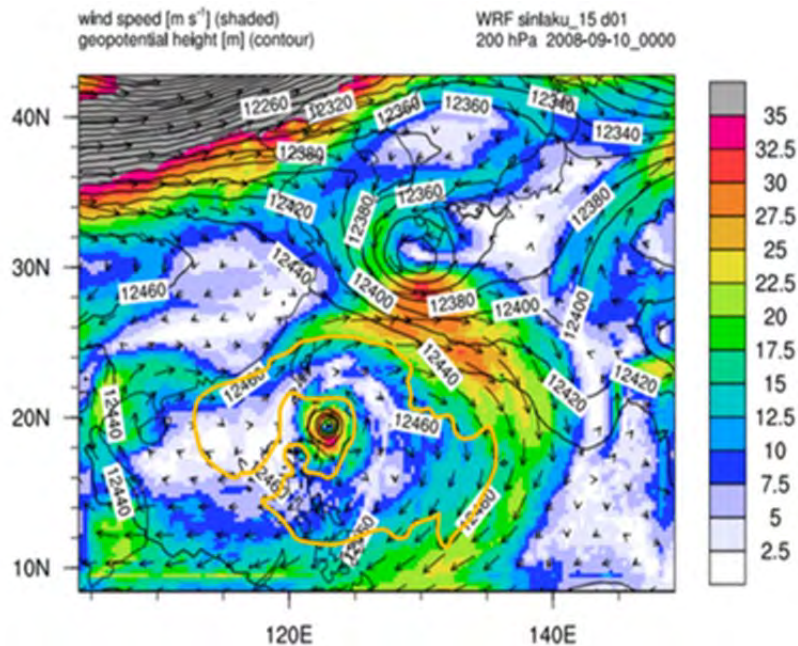


Figure 39. WRF-OPS 36-h analyzed winds (vectors), speed (m s^{-1} , shaded) at 200 hPa and 200 hPa geopotential heights (m, contours at 20 m intervals). The yellow contour represents 12,460 m geopotential heights at 0000 UTC 10 September.

Over the next 36 hours, the 72 h forecast that verified at 1200 UTC 11 September indicated that landfall on the southern end of Taiwan was imminent. Under the influence of the strong midlatitude trough, lower-level (Figure 40) and mid-level (Figure 41) ridge retreated poleward over Japan. The upper level trough (Figure 42) was moving east of Japan. As the trough moved eastward, its influence to Sinlaku weakened as Sinlaku continued to move west-northwest toward southern Taiwan.

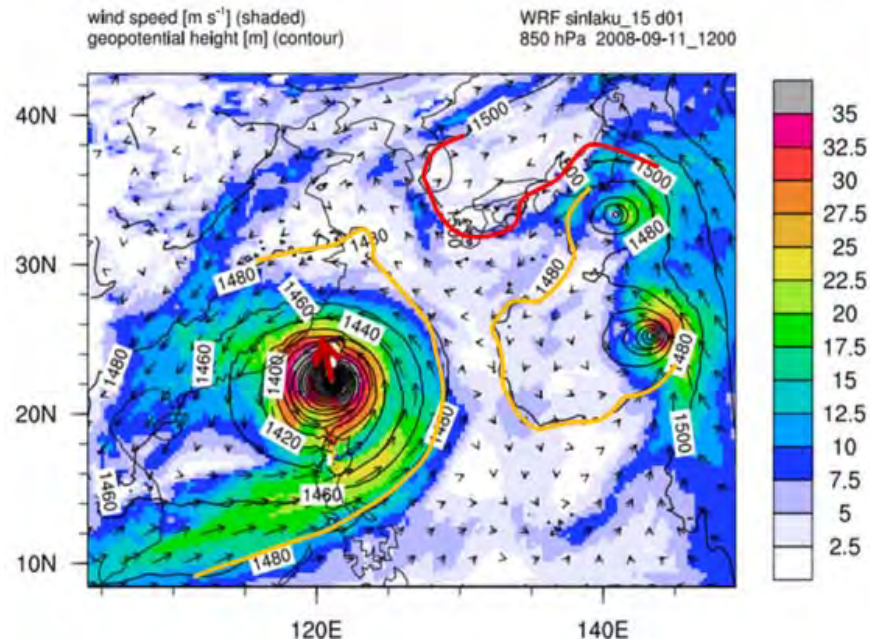


Figure 40. WRF-OPS 72-h forecast winds (vectors) and speed (m s^{-1} , shaded) at 850 hPa and 850 hPa geopotential heights (m, contours at 20 m intervals). The red vector indicates general storm motion. The red and yellow contours represent 1500 m and 1480 m geopotential heights, respectively, at 1200 UTC 11 September.

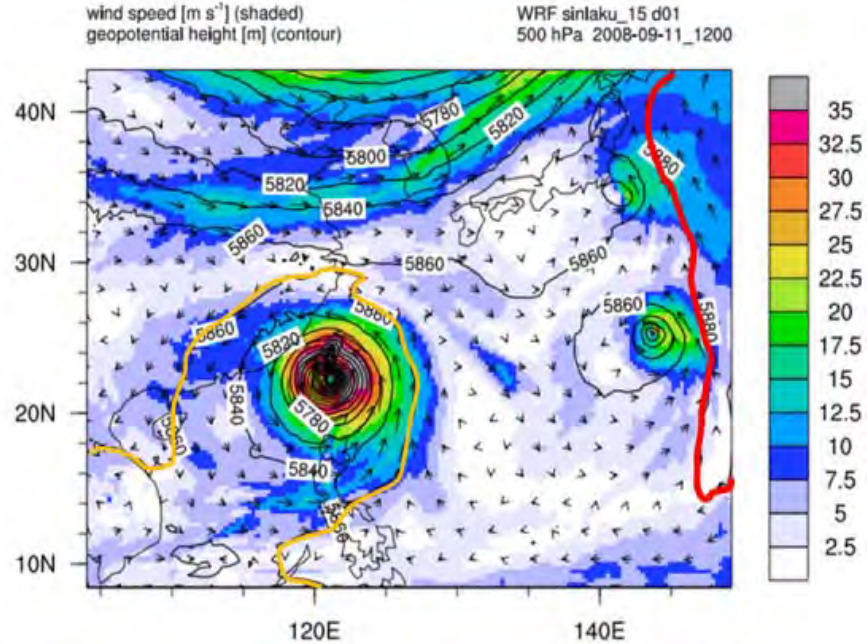


Figure 41. WRF-OPS 72-h forecast winds (vectors) and speed (m s^{-1} , shaded) and 500 hPa geopotential heights (m, contours at 20 m intervals). The red and yellow contours represent 5880 m and 5860 m geopotential heights, respectively, at 1200 UTC 11 September.

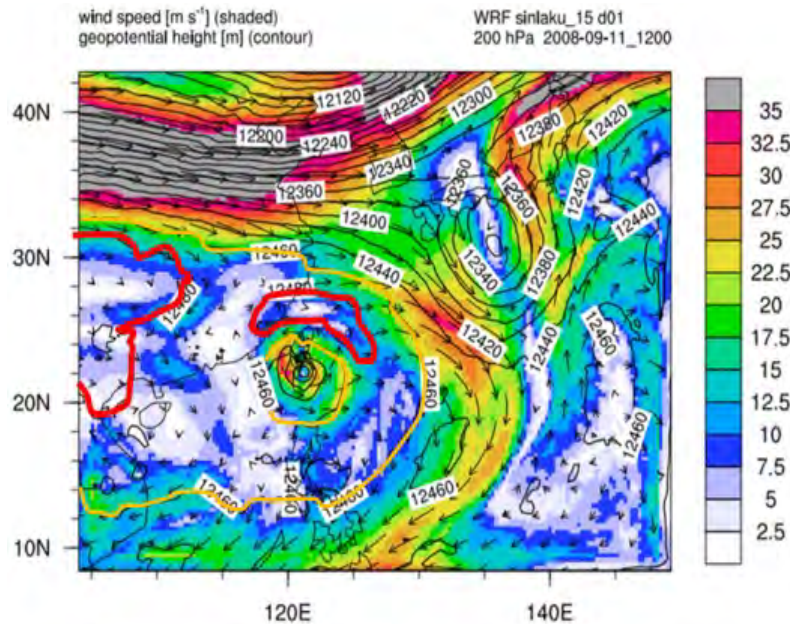


Figure 42. WRF-OPS 72-h forecast winds (vectors) and speed (m s^{-1} , shaded) at 200 hPa and 200 hPa geopotential heights (m, contours at 20 m intervals). The red and yellow contours represent 12,480 m and 12,460 m geopotential heights, respectively, at 1200 UTC 11 September.

As indicated in Figure 3, the WRF-OPS forecast track of Sinlaku was too far south than the actual track. Based on the analysis of the WRF-OPS forecast fields, the southward track was due to the subtropical ridge remaining a strong influence to the northeast of the storm. Also, the midlatitude trough moved rapidly eastward such that it did not influence Sinlaku.

B. SINLAKU WRF-DA EXPERIMENTS

In this study, three primary parameters (storm intensity, steering flow, and initial position of the storm) were examined to determine the impacts of observation and type were on the model forecasts of Sinlaku. During Sinlaku, the operational forecast uncertainty associated with storm track and intensity was high. The time and location of recurvature to the north then east was not well forecasted by the numerical weather models. It is widely held that a better initial analysis of the large-scale conditions around the storm often lead to a more accurate forecast. In an attempt to gain more confidence in the forecast, this study examined potential impacts of strategic observations. To this end, the WRF experimental model runs were produced and examined to see what impacts were made.

Various sets of observations were assimilated to define the WRF model experiments. As discussed in Chapter II, the first variant (WRF-CONV) assimilated only conventional observations into the model. The second variant (WRF-C130) assimilated both conventional observations as well as the actual WC-130J dropwindsonde data collected during T-PARC and Typhoon Sinlaku. The final variation of the WRF model run (WRF-PSEUDO) assimilated conventional observations and pseudo dropwindsonde data derived from ECMWF analysis of Sinlaku.

1. Initial Position

Many factors can be attributed to the differences among numerical forecasts. For example, storm structure and intensity can play a role as well as synoptic weather patterns. In this study, it is also important to note that each WRF simulation conducted was by design assimilated with different sets of observation. The result not only

produced different ensemble consensus, but also established different initial positions of the storm center

The experimental WRF ensemble model runs (Figure 43) indicate various degrees of uncertainty and accuracy. The degree of uncertainty, which is based on the spread among ensemble members, between WRF-CONV and WRF-PSEUDO is very similar. However, there are subtle differences. The WRF-CONV is biased toward a more southerly landfall position while the WRF-PSEUDO track ensemble average has a more northerly track. The track of WRF-CONV is closest to the WRF-OPS, which indicates that the assimilation of conventional observations is likely similar to the use of the ECMWF operational forecasts. This is consistent as the ECMWF forecast were initialized with the conventional observations. Both WRF-CONV and WRF-PSEUDO contain more track uncertainty than does WRF-C130. It is hypothesized that the WRF-C130 had the added benefit of 21 *in situ* observations of the storm center as well as conventional observation assimilation. The *in situ* observations of the storm center meant the accuracy of the storm placement during the time of the model initialization was much greater than that of WRF-CONV and WRF-PSEUDO. By having a better sense of the current storm structure, the WRF-C130 forecast produced less uncertainty and a more accurate forecast than did the model with conventional observations alone.

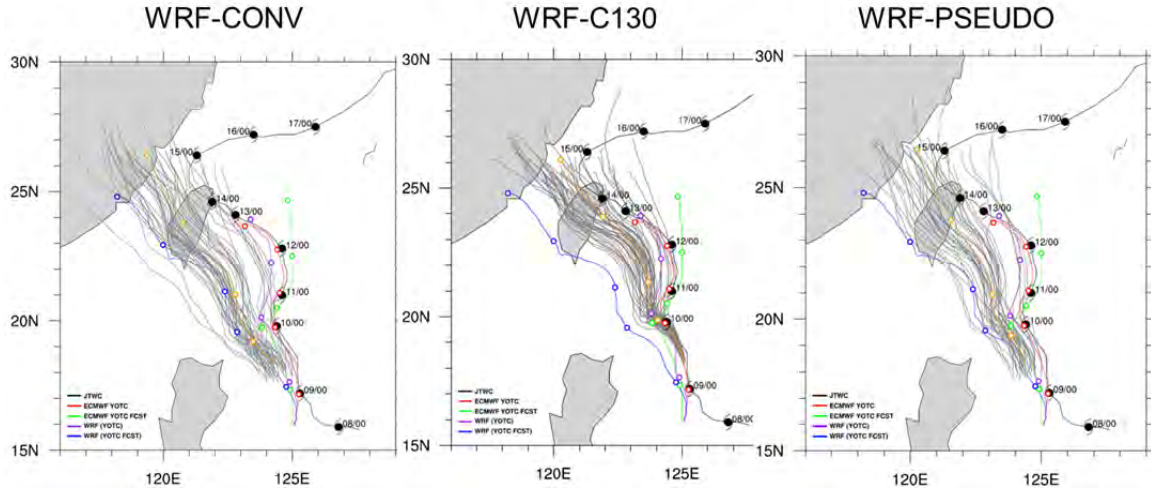


Figure 43. Ensemble WRF forecasts from the three WRF-DA experiments. Grey lines are ensemble member forecast tracks for TY Sinlaku. Orange line is the ensemble consensus. Black line is JTWC best track. Red line is ECMWF YOTC analysis. Green line is ECMWF YOTC forecast. Purple line is WRF-ANAL. Blue line is WRF-OPS forecast (no additional observation assimilation). Dots represent potential storm position for the given model in 24 h intervals.

Although WRF-PSEUDO did not lead to a more accurate forecast over WRF-C130, it was improved over WRF-CONV. In comparison, WRF-PSEUDO included conventional observations and ECMWF derived pseudo dropwindsonde observations of the upper-level outflow jet region of the storm. With only 15 additional observations along the outflow jet, the resulting forecast shifted what was a southerly track of WRF-CONV to a more northerly track of WRF-PSEUDO, thus bringing the forecast in greater alignment with the actual track.

Because the WC-130J observations were obtained at low-levels in the storm core, it is expected that assimilation of those data would yield a more accurate storm structure and initial position. Comparison of storm position between the WRF-C130 and WFD-CONV (Figure 44) defines a vorticity dipole, which is indicative of differences in position. The dipole pattern suggests that the storm was moving too quickly to the north and east in the WRF-CONV forecast. Since the experimental models started the storm in different locations and the models were built on different observation sets, the resulting

ensemble predictions were also different. The degree to which initial positional difference played in each ensemble consensus track is difficult to state, however it can be speculated that the initial position of the storm is a large contributor to the resulting accuracy of the forecast.

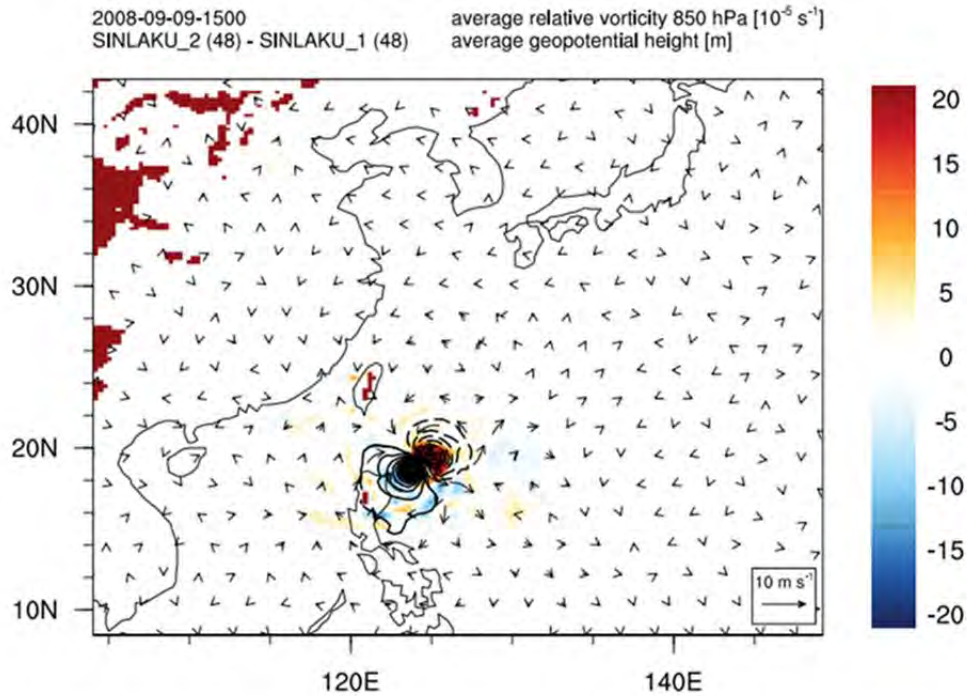


Figure 44. Vorticity difference WRF-C130 minus WRF-CONV for the 18 h forecast verified at 1500 UTC 9 September. Shading represents relative vorticity differences at 850 hPa [10^{-5} s^{-1}]. Contours represent geopotential height differences [m].

It is possible that if storm centered *in situ* observations had been successfully assimilated into WRF-PSEUDO, the resulting ensemble forecast would have been more accurate than the WRF-C130.

2. Mean Wind Steering Flow

The steering flow defined in each WRF model forecast was analyzed to help explain the forecast track differences. Wind difference fields were also examined between WRF forecasts to ascertain causes for the steering flow changes from forecast to

forecast. Holland (1984) defined steering flow as a weighted average wind between 300 and 800 hPa pressure heights extended over 5 to 7 degrees latitude from the center of rotation. Fiorino and Elsberry (1989) went further by advocating a larger annulus size of 300-1000 km from the storm center for averaging steering flow. The steering flow calculations in this study used various combinations of pressure levels and annulus sizes to generate several steering flow definitions. Among them were the parameters advocated by Holland (1984) and Fiorino and Elsberry (1989). All plots were examined carefully to determine which levels and annulus size bore the greatest resemblance to the average storm motion plot of each WRF run (Figure 45). Then the relevant atmospheric factors were considered in each WRF solution.

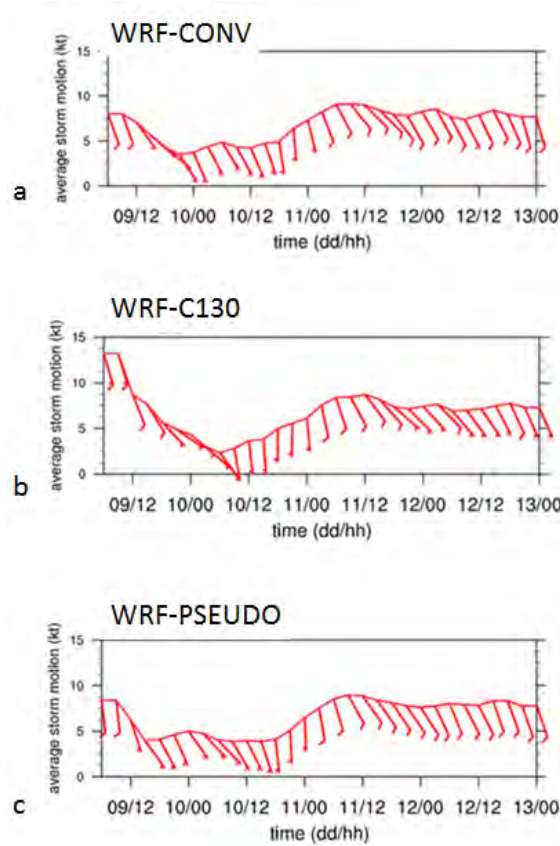


Figure 45. Average motion of Sinlaku for each WRF model run: WRF-CONV (a), WRF-C130 (b), and WRF-PSEUDO (c). The red line and wind barbs denote wind direction and magnitude in increments of 5 knots.

The times of particular interest for comparison of steering flows are centered about 0000 UTC 10 September because this was when Sinlaku began to recurve to the north-northeast for a 24 h period before ultimately turning back to the northwest for its approach to Taiwan (Figure 3).

On 8 September 2008, the track uncertainty of Sinlaku by the ECMWF Ensemble Prediction System (ECMWF EPS) models was high due in part to the weak steering flow of the storm, as well as the relatively slow speed to the north (Figure 46) It was at this critical moment in the life of Sinlaku that would determine if landfall would be in Taiwan or turn to spin out harmlessly over the western North Pacific.

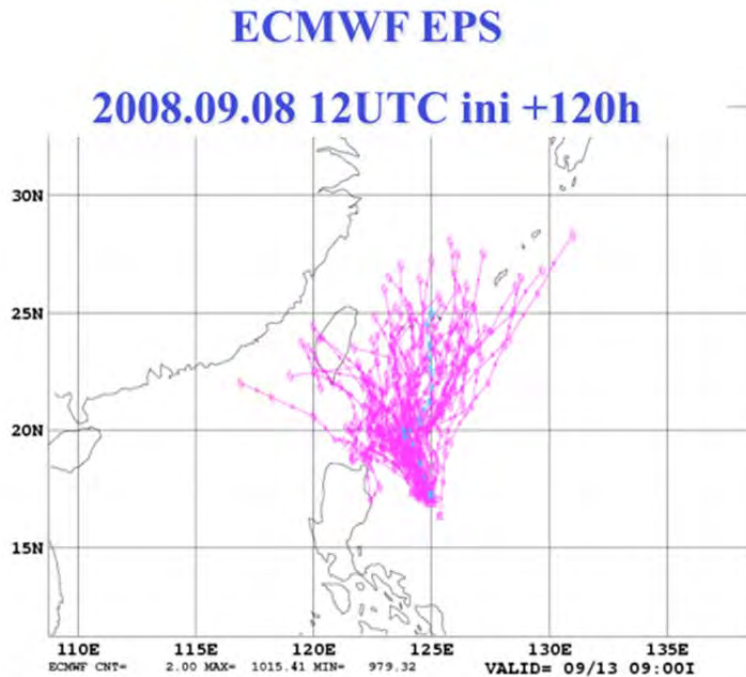


Figure 46. ECMWF EPS at 1200 UTC 8 September. Pink lines represent ensemble member tracks. (From T-PARC catalog)

The predominant feature in all steering calculations was the consistent 5-10 kt southerly flow varying from southwest to southeast (Figure 47). Subtle details can be seen upon closer examination as it relates to the different annulus sizes. However, regardless of the annulus size, it is evident in WRF-C130 and WRF-PSEUDO flow fields prior to 1200 UTC 9 September that a distinguishable southwest component existed

where none was evident in WRF-CONV (Figure 47). Presumably, the fact that neither the outflow jet nor the storm center was well captured by conventional observations was causes for WRF-CONV to track fairly continually to the west-northwest without any appreciable turn to the north.

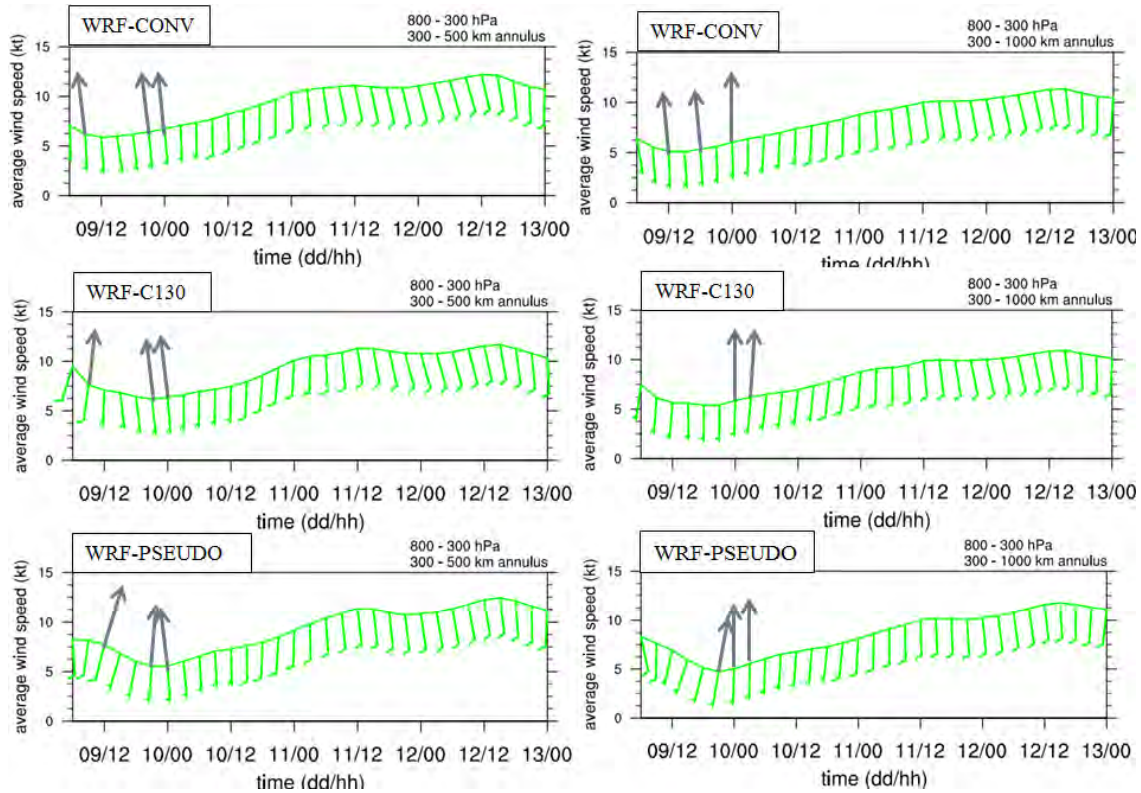


Figure 47. Average wind speed and direction at 300 - 800 hPa level with a 300-500 km (left) and 300-1000 km (right) annulus. The abscissa represents date (MM) and time (HH). The ordinate is the magnitude of the steering flow. The green line and wind barbs denote wind direction and magnitude in increments of 5 knots.

When considering WRF-PSEUDO and WRF-C130, it's important to keep in mind where the observations were collected. WRF-PSEUDO observations were collected well north of the storm center in the upper-level outflow region of the storm while WRF-C130 was collected at lower altitudes in close proximity of the storm center. Observational studies have shown that TC steering is often controlled by the average air flow 5-7

degrees from TC center (Holland, 1984). At this distance the effect of radial winds in the steering flow calculations have little influence, thus isolating a more pure steering flow.

The flow in the WRF-PSEUDO 300-1000 km annulus plots in Figure 47 look to be in better agreement with the actual turn to the north-northeast that Sinlaku took on or about 10 September than does the smaller annulus of 300-500 km. The winds just before 0000 UTC 10 Sept in the 300-500 km annulus wind calculations are somewhat opposed. In contrast, the winds in the same time period calculated at the larger annulus are more parallel and complementary to the north-northeast movement of the storm.

Ultimately, the WRF-C130 experiment provided a more accurate TC track than WRF-CONV and WRF-PSEUDO. However, it is evident that a better representation of the overall environmental structure; particularly where the dominant influence of a passing trough are concerned, resulted in improved forecasts. This was evident in the WRF-C130 and WRD-PSEUDO forecast fields discussed earlier.

By examining differences in wind fields at 200 hPa, 500 hPa, and 850 hPa it is evident that the storm outflow and the midlatitude jet were better represented by the WRF-PSEUDO forecast while the storm initial position was better represented by WRF-C130.

Comparison of the 24-h WRF-C130 (Figure 48a) and WRF-PSEUDO (Figure 48b) 850 hPa forecasts valid at 1200 UTC 9 September indicates that easterly winds to the northeast of the storm were much stronger in WRF-PSEUDO than in the WRF-C130. Furthermore, this can be seen in the difference plots (Figure 48c) where a dipole pattern north east of the storm indicates stronger easterly winds in the WRF-PSEUDO (dark blue shading). Consequently, the WRF-C130 storm track proceeded to a more northerly direction than WRF-PSEUDO. The 30-h forecast that verifies at 1800 UTC 9 September forecast (Figure 49) indicates that the 850 hPa easterly winds in the WRF-PSEUDO (Figure 48b) became less in magnitude and shifted to more southeasterly. This was more in agreement directionally with WRF-C130 (Figure 49a), however the magnitude of the flow in WRF-PSEUDO continued to be stronger (Figure 49b,c). In the 36-h forecasts that verify at 0000 UTC 10 September (Figure 50) easterly winds north-

northeast of Sinlaku began to weaken in the WRF-PSEUDO (Figure 50b) as the subtropical ridge began to weaken and shift more to the north than in WRF-C130 (Figure 50a,c). This contributed to the storm in WRF-PSEUDO to slow its movement toward the north-northwest.

The 36-h forecasts at 500 hPa that verify at 0000 UTC 10 September (Figure 51) indicate that the midlatitude cyclone to the north of Sinlaku was farther south in the WRF-C130 (Figure 51a) forecast than in the WRF-PSEUDO (Figure 51b,c). This southward extent of the midlatitude trough is consistent with the more northerly track in the WRF-C130 forecast.

At 200 hPa, the 24-h forecast that verifies at 1200 UTC 9 September indicates that the outflow directed to the north and east was much stronger in the WRF-PSEUDO (Figure 52b) than in the WRF-C130 (Figure 52a,c). This clearly demonstrates the potential effect of upper level observations in the remote regions of a TC as defined by the location of the pseudo dropwindsondes in Figure 52b. By the 30-h forecast that verifies at 1800 UTC 9 September (Figure 53), the merger of the midlatitude trough and outflow continued to be stronger in the WRD-PSEUDO (Figure 53b) than in the WRF-C130 (Figure 53a,c). The stronger outflow at upper levels may be related to the fact that the circulation of Sinlaku at low levels is larger in the WRF-PSEUDO forecasts than the WRF-C130 forecasts. In the 36-h forecasts, the pattern of stronger outflow in the WRF-PSEUDO (Figure 54b) and greater merger between outflow and the midlatitude trough than in the WRD-C130 (Figure 54a,c) continued.

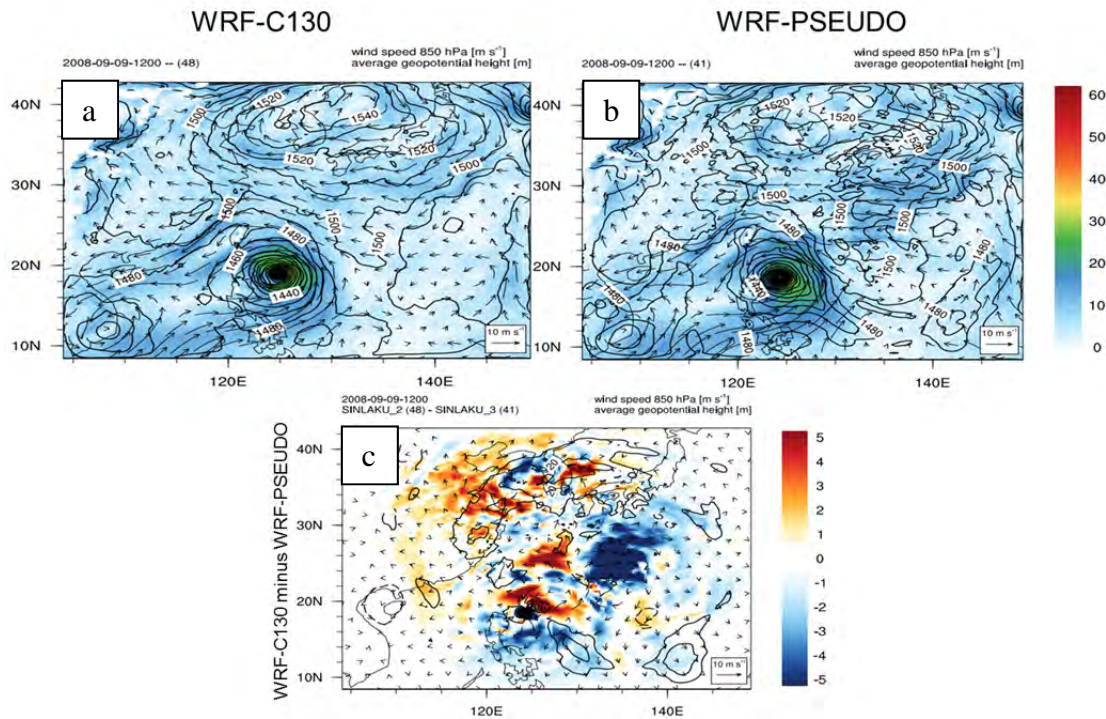


Figure 48. The 24-h forecast winds (vectors) and speed (m s⁻¹, shaded) at 850 hPa and 850 hPa geopotential heights (m, contours at 20 m intervals) that verify at 1200 UTC 9 September from the (a) WRF-C130 and (b) WRF-PSEUDO, and (c) WRF-C130 minus WRF-PSEUDO forecast differences.

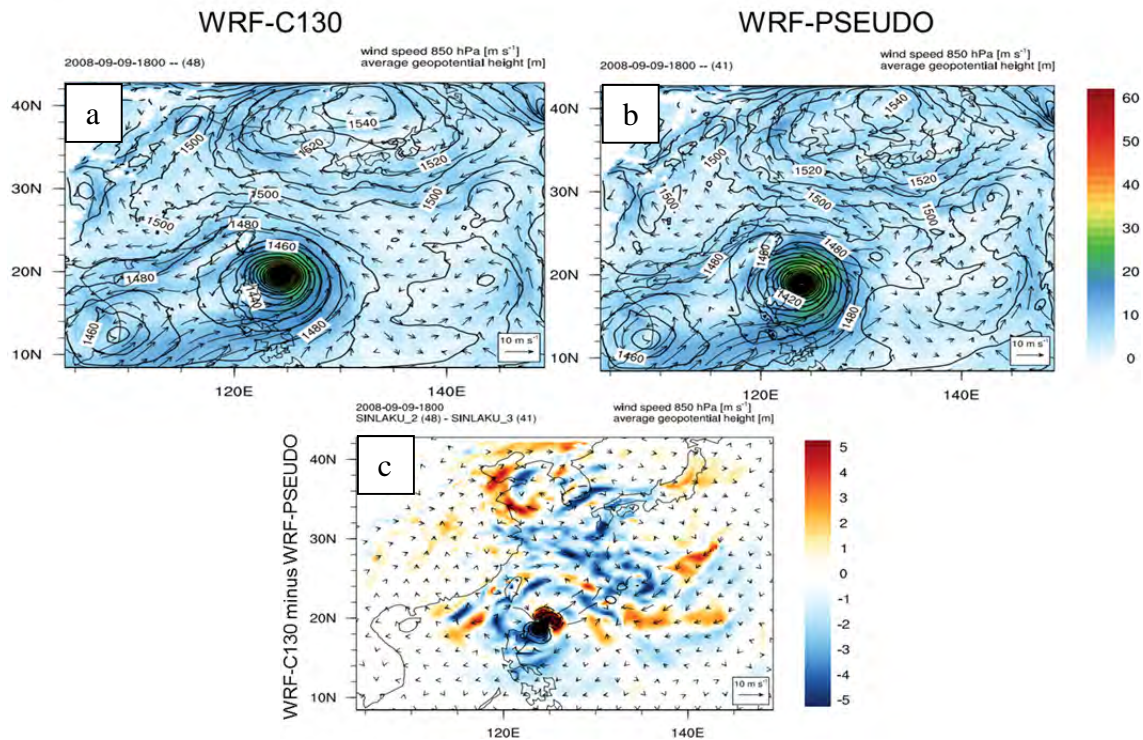


Figure 49. The 30-h forecast winds (vectors), and speed (m s^{-1} , shaded) at 850 hPa and 850 hPa geopotential heights (m, contours at 20 m intervals) that verifies at 1800 UTC 9 September from the (a) WRF-C130, (b) WRF-PSEUDO, and the (c) WRF-C130 minus WRF-PSEUDO forecast differences .

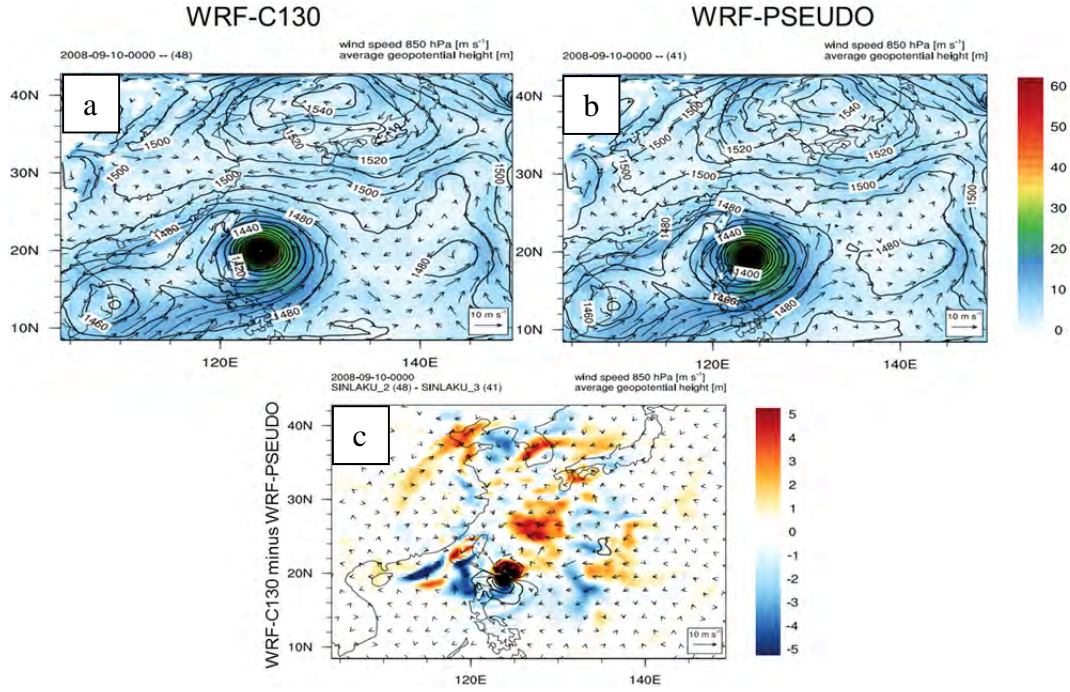


Figure 50. The 36-h forecast winds (vectors) and speed (m s^{-1} , shaded) at 850 hPa and 850 hPa geopotential heights (m, contours at 20 m intervals) that verifies at 0000 UTC 10 September from the (a) WRF-C130, (b) WRF-PSEUDO, and (c) WRF-C130 minus WRF-PSEUDO forecast differences.

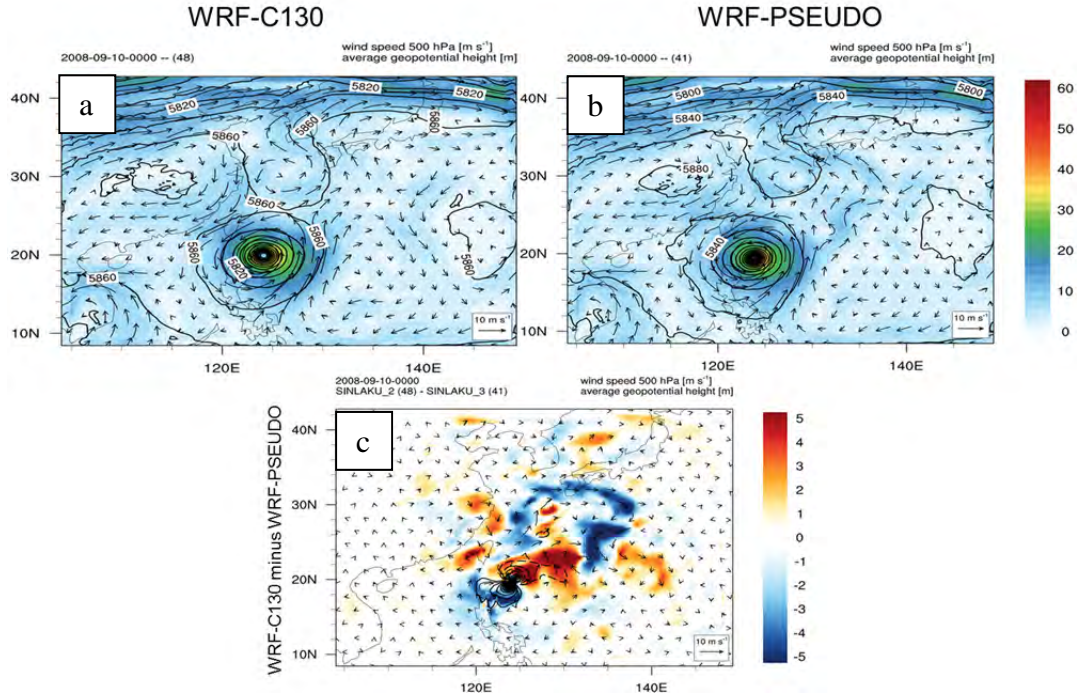


Figure 51. The 36-h forecast winds (vectors) and speed (m s^{-1} , shaded) at 500 hPa and 500 hPa geopotential heights (m, contours at 20 m intervals) that verify at 0000 UTC 10 September from the (a) WRF-C130, (b) WRF-PSEUDO, and (c) WRF-C130 minus WRF-PSEUDO forecast differences.

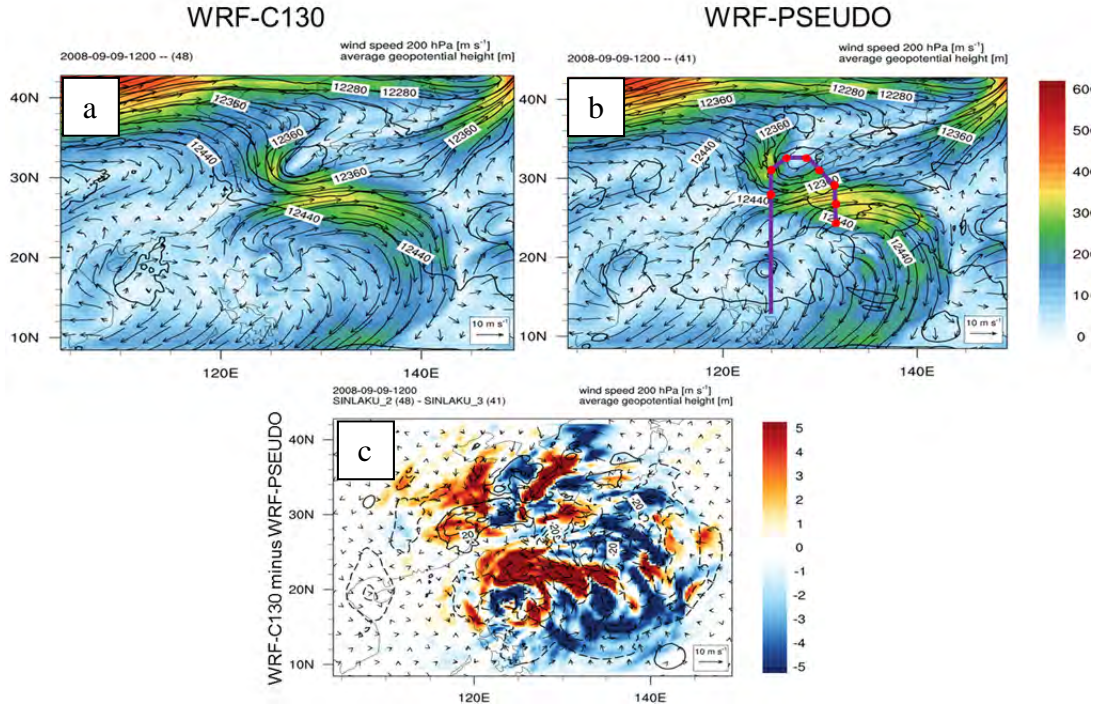


Figure 52. The 24-h forecast winds (vectors) and speed (m s^{-1} , shaded) at 200 hPa and 200 hPa geopotential heights (m, contours at 20 m intervals) that verify at 1200 UTC 9 September from the (a) WRF-C130, (b) WRF-PSEUDO, and (c) WRF-C130 minus WRF-PSEUDO forecast differences.

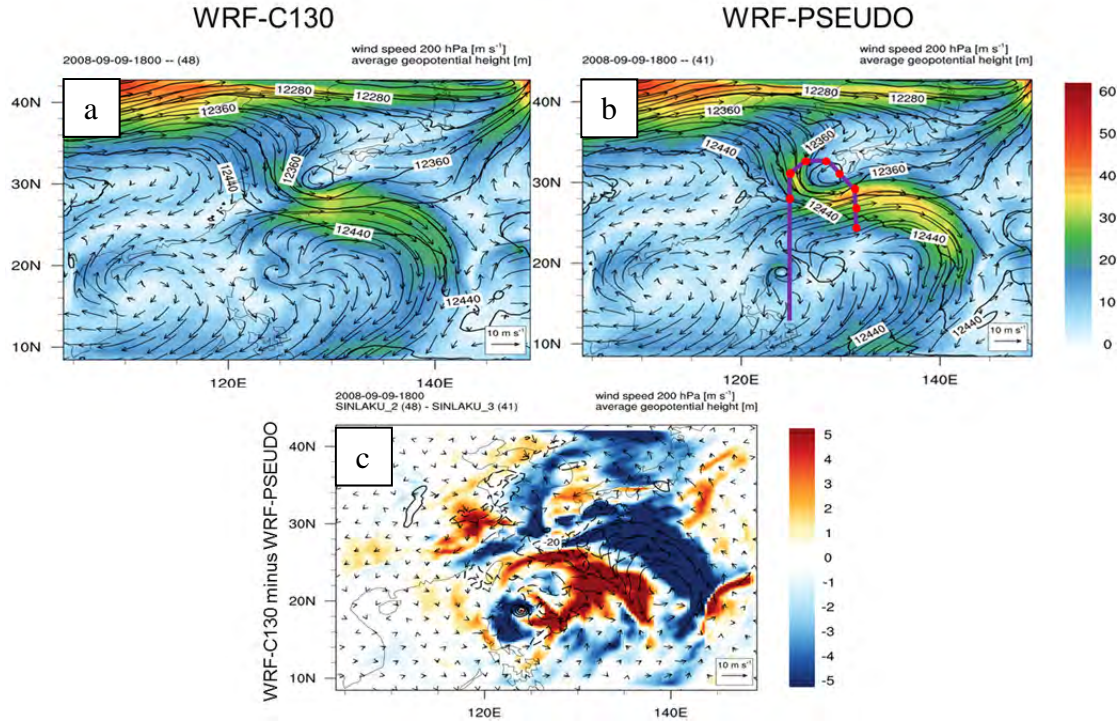


Figure 53. The 30-h forecast winds (vectors) and speed (m s^{-1} , shaded) at 200 hPa and 200 hPa geopotential heights (m, contours at 20 m intervals) that verify at 1800 UTC 9 September from the (a) WRF-C130, (b) WRF-PSEUDO, and (c) WRF-C130 minus WRF-PSEUDO forecast differences.

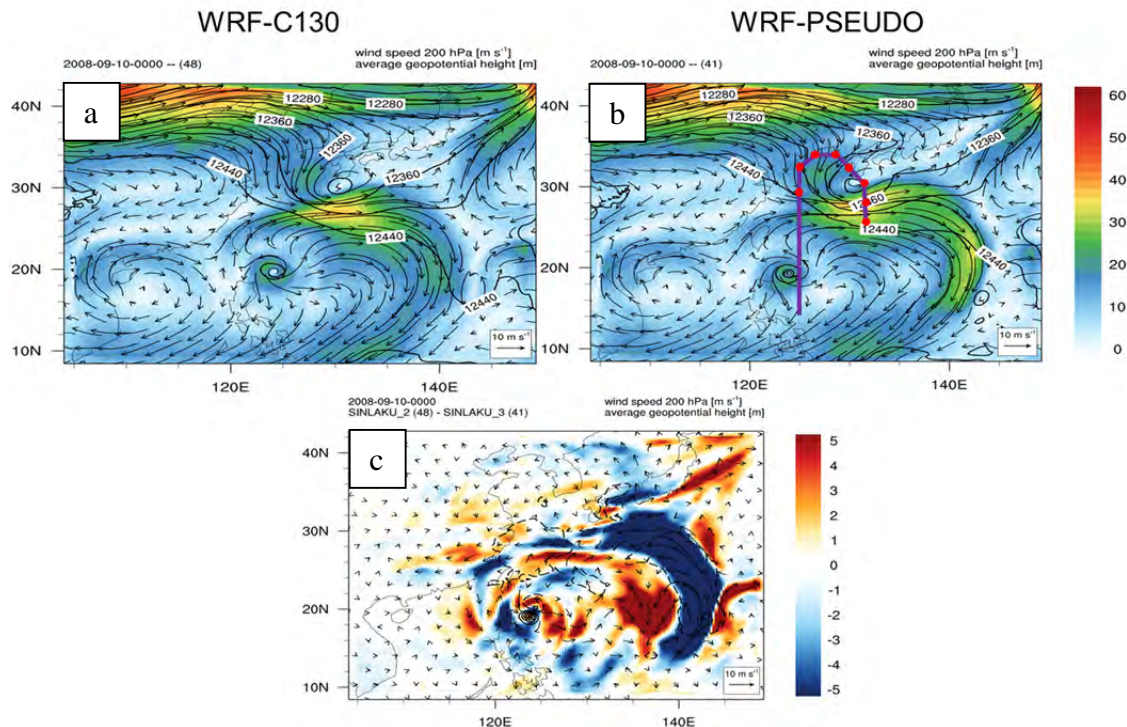


Figure 54. The 36-h forecast winds (vectors) and speed (m s^{-1} , shaded) at 200 hPa and 200 hPa geopotential heights (m, contours at 20 m intervals) that verify at 0000 UTC 10 September from the (a) WRF-C130, (b) WRF-PSEUDO, and (c) WRF-C130 minus WRF-PSEUDO forecast differences.

3. Storm Structure and Intensity

The MSLP for each of the experimental WRF runs varied (Figure 55). Unlike the track forecasts, WRF-PSEUDO resulted in the most accurate MSLP forecasts than the WRF-C130, or WRF-CONV. The members of WRF-CONV and WRF-C130 maintained a fairly constant spread until around 0000 UTC 11 September. The WRF-PSEUDO members however did not begin to lose accuracy until later in the period at 1200 UTC 11 September (Figure 55c). It is hypothesized that the increased accuracy in storm intensity in the WRF-PSEUDO is related to the stronger outflow from the storm. Perhaps, the addition of pseudo observations at upper levels in the midlatitude trough and outflow yielded better initial conditions of the environmental in that key storm-environment interaction.

As with the track forecasts, by more accurately establishing the state of the upper level trough and outflow jet region of Sinlaku in WRF-PSEUDO was better able to forecast the MSLP than WRF-CONV where only conventional observations were assimilated.

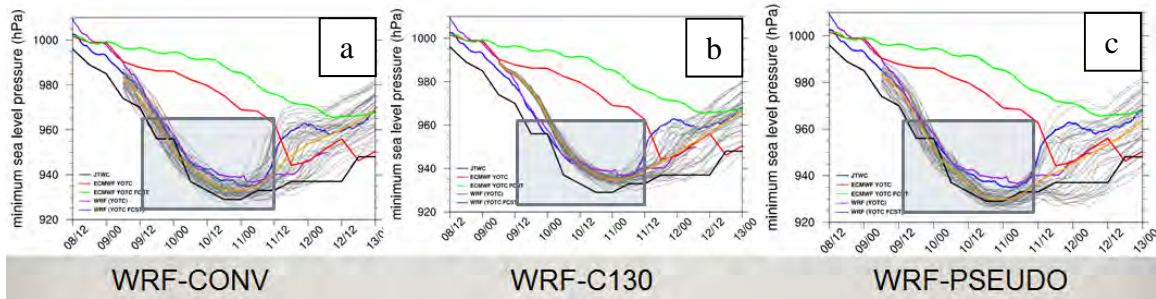


Figure 55. Forecasts of the intensity of TY Sinlaku intensity for the (a) WRF-CONV, (b) WRF-C130, and (c) WRF-PSEUDO forecasts. The grey lines define the ensemble forecasts and the orange line is the ensemble consensus. The black, red, green, purple, and blue lines represent JTWC best track, ECMWF YOTC analysis, ECMWF YOTC forecast, WRF-ANAL, and WRF-OPS, respectively. The abscissa is date (MM) and time (HH UTC). The ordinate is minimum sea level pressure (hPa) in 5 hPa increments.

THIS PAGE INTENTIONALLY LEFT BLANK

V. CONCLUSION

The mission of U. S. Naval Meteorology and Oceanography Command (METOC) has long been centered on providing the warfighter with the very best environmental information they need to make the most informed decision. To that end, this thesis set out to provide a qualitative example of how a better representation of the current atmosphere could provide more accurate forecasts. The western North Pacific relies heavily on satellite data for atmospheric observations. Although remote sensing is very accurate and has been of great service to modern day meteorologist, challenges remain.

A. SUMMARY OF FINDINGS

The goal of this thesis was to build on work done by The Observing System Research and Predictability Experiment (THORPEX) and more specifically, the THORPEX-Pacific Asian Regional Campaign (T-PARC) that was conducted in the fall of 2008 (Elsberry and Harr 2008). By using the data obtained during T-PARC, we were able to show that with only 15 additional upper level observations, strategically collected in the outflow region of a TC EPS could be benefited.

Comparisons were made between three experimental WRF model forecasts that were initialized at 1200 UTC 8 September and extended to 0000 UTC 13 September 2008. First, WRF-CONV assimilated only conventional observations. The second forecast assimilated conventional and WC-130J dropwindsonde observations that were collected in Sinlaku during T-PARC. Finally, WRF-PSEUDO assimilated the same conventional observations as WRF-CONV plus pseudo dropwindsonde atmospheric vertical profiles derived from ECMWF analysis. The pseudo dropwindsondes were designed around a hypothetical Global Hawk flight deploying dropsondes from 60,000 ft. All WRF runs were initialized by ECMWF operational forecast valid 1200 UTC 8 September, as it would have been the best representation of the forecast if an actual flight plan had been performed.

The WRF-CONV forecast was less accurate than the other two forecast models. The WRF ensemble consensus tracked the storm to the southern side of Taiwan. In

addition, the minimum sea level pressure was not as low as the other experimental runs (WRF-C130 and WRF-PSEUDO). In the WRF-CONV, the initial position of the storm was not well characterized. One of the reasons for this could be that the conventional observations alone did not capture the state of the environment as well as it good have.

By examining WRF-C130 in light of WRF-CONV a much better initial placement of the storm center existed in the initial condition. This was due in large part by *in situ* dropwindsonde observations collected by the C-130 reconnaissance flight. More accurate initial placement served to reduce track error over time when compared to the other two forecasts. Although the MSLP was closer to reality at 935 hPa, it was still higher than the actual MSLP of 929 hPa.

The initial placement continued to be an issue with the WRF-PSEUDO forecast. Initial errors in the placement of the storm center translated throughout the forecast period. However, by providing a more accurate representation of the upper atmosphere and the midlatitude jet and storm outflow jet interaction, WRF-PSEUDO was able to provide a more accurate MSLP of 930 hPa at 0000 UTC 11 September. In addition, by better forecasting the dominant steering trough to the north of Sinlaku, the ensemble consensus track resulted in a more accurate northern landfall in Taiwan than WRF-CONV.

The results of this study have offered valuable evidence into the importance of strategically place observation assimilation into numerical weather prediction. Although the experimental pseudo run, (WRF-PSEUDO) in this study fell short of the track accuracy WRF-C130, improvements nevertheless could be seen. WRF-CONV, with its sporadic conventional observation DA, was improved upon by the addition of a mere 15 strategically procured observations in the upper levels (WRF-PSEUDO). Also, WRF-PSEUDO provided a much more accurate forecast of the storm intensity than the other run. This was also owed to the well captured state of the upper levels. It is hypothesized that a combination of observations over the storm center and in the environment would provide the best components of the WRF-C130 and WRF-PSEUDO forecasts.

B. RECOMMENDATIONS FOR FURTHER STUDY

Forecasts of tropical cyclone track and intensity have long experienced large uncertainties. The sources of uncertainty can be numerous. In this study, a limited experiment suite was conducted to assess the role of observation distribution on forecast uncertainty. In this initial study, observations in the inner core of the storm led to the most accurate track forecast. However, observations from the lower stratosphere in storm outflow and midlatitude circulations lead to a better intensity forecast.

It is recommended that additional experiments be conducted to test the value of both inner core and remote observations. All of these observations, including those in the inner core, should be from high altitudes. Additionally, additional experiments could be conducted to test sensitive regions determined via methods used to objectively define regions in which there is observation sensitivity (i.e., adjoint methods, singular vectors).

THIS PAGE INTENTIONALLY LEFT BLANK

LIST OF REFERENCES

- Anderson, J. L., 2003: A local least squares framework for ensemble filtering. *Mon. Wea. Rev.*, **131**, 634–642.
- Anderson, J., L., 2007: An adaptive covariance inflation error correction algorithm for ensemble filters. *Tellus A*, **59**, 210–224. doi: 10.1111/j.1600-0870.2006.00216.
- Anderson, J., T. Hoar, K. Raeder, H. Liu, N. Collins, R. Torn, and A. Avellano, 2009: The data assimilation research test bed: A community facility. *Bull. Amer. Meteor. Soc.*, **90**, 1283–1296.
- Atkinson, R., 2012: Tropical Cyclone Reconnaissance Over the Western North Pacific with the Global Hawk: Operational Requirements, Benefits, and Feasibility. MS thesis, Dept. of Meteorology, Naval Postgraduate School, 95 pp. [Available at https://calhoun.nps.edu/bitstream/handle/10945/17315/12Sep_Atkinson_Robert.pdf?sequence=1]
- Chou, K., C. Wu, P. Lin, S. D. Aberson, M. Weissmann, F. Harnisch, and T. Nakazawa, 2011: The Impact of Dropwindsonde Observations on Typhoon Track Forecasts in DOTSTAR and T-PARC. *Mon. Wea. Rev.*, **139**, 1728–1743.
- Elsberry, R. L., and P. A. Harr, 2008: Tropical cyclone structure (TCS2008) field experiment: science basis, observational platforms, and strategy. *Asia-Pacific J. Atmos. Sci.*, **44**, 122–143.
- Fiorino, M. and R. L. Elsberry, 1989: Some Aspects of Vortex Structure Related to Tropical Cyclone Motion. *J. Atmos. Sci.*, **46**, 975–990, doi:10.1175/1520-0469(1989)046<0975:SAOVS>2.0.CO;2.
- Fritsch, J. M. and J. S. Kain, 1993: Convective parameterization for mesoscale models: The Fritsch–Chappell scheme. *The Representation of Cumulus Convection in Numerical Models, Meteor. Monogr.*, No. **46**, Amer. Meteor. Soc., 159–164.
- Gaspari, G. and S. E. Cohn, 1999: Construction of correlation functions in two and the dimensions. *Q. J. R. Meteorol. Soc.*, **125**, 723–757. doi: 10.1002/qj.49712555417
- Gleick, J., 1987: *Chaos: Making a New Science*. Penguin Books, 384 pp.
- Hamill, T. M., J. S. Whitaker, and S. L. Mullen, 2006: Reforecasts: An important dataset for improving weather predictions. *Bull. Amer. Meteor. Soc.*, **87**, 33–46.
- Harr, P. A. 2011: Tropical cyclone reconnaissance with the Global Hawk: operational requirements, benefits, and feasibility. *CRUSER Newsletter*, October. [Available at <http://www.nps.edu/CRUSER>.]

- Hong, S. Y. and J. O. J. Lim, 2006: The WRF single-moment 6-class microphysics scheme (WSM6). *J. Korean Meteor. Soc.*, **42**, 129–151.
- Hong, S.-Y., Y. Noh, and J. Dudhia, 2006: A new vertical diffusion package with an explicit treatment of entrainment processes. *Mon. Wea. Rev.*, **134**, 2318–2341.
- Holland, G. J., 1984: Tropical Cyclone Motion. A Comparison of Theory and Observation. *J.Atmos.Sci.*, **41**, 68-75, doi:10.1175/1520-0469(1984)041<0068:TCMACO>2.0.CO;2.
- JTWC, 2008: Annual Tropical Cyclone Report. [Available at <http://jtwccdn.appspot.com/NOOC/nmfc-ph/RSS/jtwc/atcr/2008atcr.pdf>.] 116 pp.
- Kain, J. S., 2004: The Kain–Fritsch convective parameterization: An update. *J. Appl. Meteor.*, **43**, 170–181.
- Lorenz, E. N., 1963: Deterministic Nonperiodic Flow. *J.Atmos.Sci.*, **20**, 130-141, doi:10.1175/1520-0469(1963)020<0130:DNF>2.0.CO;2.
- Majumdar, S. J. and Co-authors, 2001: Targeted Observations for Improving Numerical Weather Prediction: An Overview, 15.
- Montgomery, M. T., L. L. Lussier III, R. W. Moore, and Z. Wang, 2008: The genesis of Typhoon Nuri as observed during the Tropical Cyclone Structure 2008 (TCS-08) field experiment – Part 1: The role of the easterly wave critical layer, *Atmos. Chem. Phys.*, **10**, 9879-9900. [Available at <http://www.atmos-chem-phys.net/10/9879/2010/acp-10-9879-2010.pdf>]
- Raymond, D. J. and C. López Carrillo: 2011: The vorticity budget of developing typhoon Nuri (2008), *Atmos. Chem. Phys.*, **11**, 147-163, doi:10.5194/acp-11-147-2011.
- Richardson, L. F., 1965: *Weather Prediction by Numerical Process*. Dover Publications, 229 pp.
- Saha, S., S. Moorthi, H. Pan, X. Wu, J. Wang, S. Nadiga, P. Tripp, R. Kistler, J. Woollen, D. Behringer, H. Liu, D. Stokes, R. Grumbine, G. Gayno, J. Wang, Y. Hou, H. Chuang, H. H. Juang, J. Sela, M. Iredell, R. Treadon, D. Kleist, P. Van Delst, D. Keyser, J. Derber, M. Ek, J. Meng, H. Wei, R. Yang, S. Lord, D. D. Van, A. Kumar, W. Wang, C. Long, M. Chelliah, Y. Xue, B. Huang, J. Schemm, W. Ebisuzaki, R. Lin, P. Xie, M. Chen, S. Zhou, W. Higgins, C. Zou, Q. Liu, Y. Chen, Y. Han, L. Cucurull, R. W. Reynolds, G. Rutledge, and M. Goldberg, 2010: The NCEP Climate Forecast System Reanalysis. *Bull.Amer.Meteor.Soc.*, **91**, 1015-1057, doi:10.1175/2010BAMS3001.1.

- Sanabia, E. R., 2010: The re-intensification of Typhoon Sinlaku (2008). PHD dissertation, Dept. of Meteorology, Naval Postgraduate School, 233 pp.
[Available at
http://edocs.nps.edu/npspubs/scholarly/dissert/2010/Jun/10Jun_Sanabia_PhD.pdf]
- Skamarock, W. C., and Coauthors, 2008: A description of the Advanced Research WRF version 3. NCAR Tech. Note NCAR/TN-475+STR, 113 pp,
doi:10.5065/D68S4MVH
- Stephen, T., 2010: Tropical Cyclone Operations in U.S. Pacific Command (USPACOM). USPACOM Instruction 0539.1.
- Waliser, D. E., and Coauthors, 2012: The “year” of tropical convection (May 2008 to April 2010): Climate variability and weather highlights. *Bull. Amer. Meteor. Soc.*, **93**, 1189–1218.
- Weissmann, M., R. H. Langland, C. Cardinali, P. M. Pauley, and S. Rahm, 2012: Influence of airborne Doppler wind lidar profiles near Typhoon Sinlaku on ECMWF and NOGAPS forecasts. *Q. J. R. Meteorol. Soc.*, **138**, 118–130,
doi:10.1002/qj.896.
- Weissmann, M., F. Harnisch, C.-C. Wu, P.-H. Lin, Y. Ohta, K. Yamashita, Y.-H. Kim, E.-H. Jeon, T. Nakazawa, and S. Aberson, 2011: The influence of assimilating dropwindsonde data on typhoon track and midlatitude forecasts. *Mon. Wea. Rev.*, **139**, 908–920. doi:10.1175/2010MWR3377.1.

THIS PAGE INTENTIONALLY LEFT BLANK

INITIAL DISTRIBUTION LIST

1. Defense Technical Information Center
Ft. Belvoir, Virginia
2. Dudley Knox Library
Naval Postgraduate School
Monterey, California